

Dynamics in an Idealized Ionic Liquid Model

Durba Roy, Nikhil Patel,[†] Sean Conte,[‡] and Mark Maroncelli*

Department of Chemistry, The Pennsylvania State University, University Park, Pennsylvania 16802

Received: January 18, 2010; Revised Manuscript Received: April 13, 2010

An idealized four-site ionic liquid model having characteristics approximating those of 1-butyl-3-methylimidazolium hexafluorophosphate ([Im₄₁][PF₆]) is introduced as a low-cost alternative to existing all-atom models for purposes of simulating solute-based dynamics over nanosecond and longer time scales. The structural and energetic properties of the model are in reasonable agreement with those of [Im₄₁][PF₆] and similar ionic liquids, but the dynamics are unrealistically slow. A temperature shift of ~100 K is required to produce agreement between the viscosity and diffusion coefficients of the model and experimental values. Several aspects of the ion dynamics such as subdiffusive translational motions, non-Gaussian van Hove distributions, and jumplike displacements in both positions and orientations, are similar to behavior observed in supercooled liquids. Translational diffusion coefficients and rotational correlation times show roughly the proportionalities to viscosity expected from hydrodynamic models, and slip hydrodynamic calculations provide reasonable accuracy in some cases. But anomalously high rotational diffusion coefficients which decouple from viscosity at low temperature are also observed. These anomalies are explained in terms of the prevalence of 180° rotational jumps coupled to the presence of marked heterogeneity in rotational motions, especially about one molecular axis. Comparisons between the dynamics observed in the ionic liquid (IL) model and a neutral mixture (NM) counterpart help to explain the origins of the distinctive dynamics in ionic liquids compared to conventional solvents. The requirement for balancing electrostatic interactions in the IL leads to uniform and interleaved distributions of cations and anions resembling a distorted ionic lattice, similar to the structure of molten NaCl. The resistance to reorganizing this structure is what leads to the slow dynamics of ionic liquids. The coupling among large collections of ions is presumably responsible for the similarity of ionic liquids to supercooled conventional liquids.

1. Introduction

By virtue of their potential utility, as well as for their intrinsic interest as a new type of liquid medium, room-temperature ionic liquids (ionic liquids for short) have been vigorously studied over the past decade.^{1–8} Computer simulations have contributed significantly to this effort and have helped to shape our understanding of the distinctive physical properties of these liquids and their behavior as solvent media.^{9–18} A number of groups have laid the foundations for simulation work by developing and characterizing transferrable force fields for molecular simulations^{19–26} of ionic liquids. The earliest attempts at force-field development^{27–29} showed that minor modification of general-purpose force fields was sufficient to provide reasonable predictions for static properties such as densities, compressibilities, and thermal expansion coefficients of neat ionic liquids. Solution and dynamical properties have required more refinement of intermolecular potentials. For example, it is now appreciated that properties such as diffusion coefficients, viscosity, and conductivity of the neat liquids are fairly sensitive to details of the force field, such that 10-fold or larger errors are common in otherwise acceptable models.^{30,26,31,32} Nevertheless, recent efforts by a number of groups have shown that careful parametrization or fine-tuning of existing models can create all-atom force fields capable of high fidelity for reproducing both

static and dynamic properties of neat ionic liquids^{33,23,30,26} as well as in modeling mixtures of ionic liquids with other molecules.^{34,11,35,36,18}

Our group is specifically interested in dynamical aspects of solvation and their effect on intra- and intermolecular electron transfer in ionic liquids, which we have studied using fluorescence methods.^{37–39} To aid in the correct molecular interpretation of these experiments, we have initiated computer simulations of the same processes. While a number of insightful simulations of solvation dynamics^{40–42,14,43–46} and some aspects of electron-transfer reactions in ionic liquids^{47–49} have already been reported, these simulations have only explored the equilibrium or short-time (<100 ps) aspects of these phenomena, whereas the experiments typically measure dynamics on the 10 ps to 100 ns time scale. The reason for this discrepancy is simply that the long (~1 μs) trajectories required to collect information on the nanosecond dynamics of dilute solutes makes such simulations prohibitively costly using all-atom force fields. For this reason, we have developed an idealized simulation model which can be used to supplement more realistic all-atom simulations of ionic liquids for the purpose of simulating solute-based dynamics on nanosecond and longer time scales.

The model is similar in spirit to the coarse-grained models of alkyl imidazolium ionic liquids developed by the groups of Balasubramanian et al.^{50,51} and Voth et al.^{52,53} for studying polar/apolar aggregation phenomena. But it is even simpler than the latter models, consisting of a single-site anion and a three-site cation patterned crudely after 1-butyl-3-methylimidazolium hexafluorophosphate. (Hereafter we refer to this liquid as “[Im₄₁][PF₆]” and other 1-alkyl-3-methyl imidazolium cations

* To whom correspondence should be addressed.

[†] Current address: Emory University School of Law, 1301 Clifton Rd NE, Atlanta, Georgia 30322.

[‡] Current address: Department of Chemistry and Chemical Biology, Cornell University, Baker Laboratory, Ithaca NY 14853-1301.

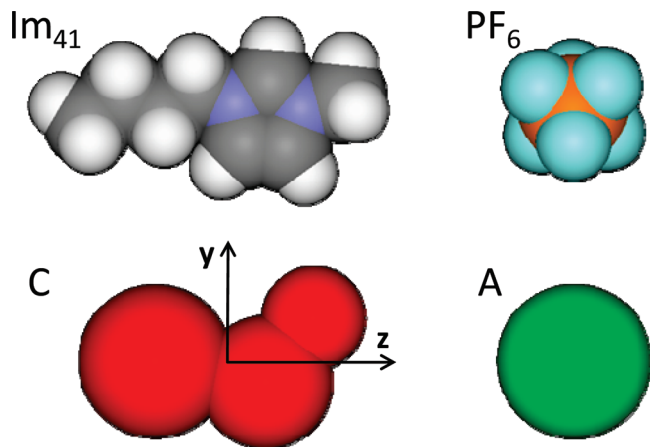


Figure 1. Space-filling representations of $[\text{Im}_{41}][\text{PF}_6]$ and the idealized model examined here.

by “ Im_{n1}^+ ” with n denoting the alkyl chain length.) In contrast to the approach of the former groups, especially that of Voth and co-workers who used force-matching to find the optimum coarse-grained representation of a specific ionic liquid, $[\text{Im}_{21}][\text{NO}_3]$,⁵⁴ we only used the prototypical ionic liquid $[\text{Im}_{41}][\text{PF}_6]$ as a reference point for creating a generic model which is representative of common ionic liquid behavior. Such a generic model is suitable for our purposes because the specific characteristics of individual ionic liquids have been shown to have little influence over the dynamics of interest to us.³⁸ Thus, the attributes of the model anion and cation were chosen to mimic the sizes and shapes of PF_6^- and Im_{41}^+ and the short-ranged components of the model coarsely tuned to reproduce the density of $[\text{Im}_{41}][\text{PF}_6]$ near room temperature. Thereafter, we examined the properties of the model liquid to judge its realism without further tuning.

In the present work we discuss the equilibrium and dynamic features of the model so constructed. Its use in solute-based simulations will be described in a forthcoming report. Section 2 of the present paper describes the model and the simulation methods employed. In section 3, we compare properties of the model liquid to experiments as well as to all-atom simulations of $[\text{Im}_{41}][\text{PF}_6]$ in order to assess its suitability as a representation of this specific ionic liquid and as a generic ionic liquid model. In section 4 we examine the nature of the translational and rotational motion of ions in this system and compare the simulated dynamics to expectations of hydrodynamic theories. Finally, in section 5 we compare equilibrium and dynamical properties of the model ionic liquid to the equivalent “neutral mixture” (NM) in which all electrostatic interactions are removed. This comparison, inspired by the insightful experiments of Shirota and Castner,⁵⁵ provides some useful perspectives on how ion–ion interactions render ionic liquids distinct from conventional organic solvents.

2. Model and Simulation Methods

As already mentioned, the goal of the present study was to generate an idealized model that captures many of the essential features of the ionic liquids as solvents while being simple enough to be computationally economical. For this purpose we chose the four-site Lennard-Jones (6–12) plus Coulomb representation illustrated in Figure 1 and detailed in Table 1. Anion A consists of a single site the size of PF_6^- and cation C of three sites chosen to coarsely represent the imidazole ring and the butyl and methyl groups of Im_{41}^+ . The sizes and charges of

TABLE 1: Model Parameters^a

site i	$x/\text{\AA}$	$y/\text{\AA}$	$z/\text{\AA}$	m/m_u	$\sigma_i/\text{\AA}$	$\varepsilon_i/(\text{kJ mol}^{-1})$	q/e
C_1 (“Im”)	0	−0.527	1.365	67.07	4.52	2.56	0.5608
C_2 (“Me”)	0	1.641	2.987	15.04	3.51	0.36	0.2024
C_3 (“Bu”)	0	0.187	−2.389	57.12	5.20	1.83	0.2367
A(“ PF_6^- ”)	0	0	0	144.96	5.22	4.71	−1

^a Site–site interaction energies are of the form $u_{ij}(r_{ij}) = 4\varepsilon_{ij}\{(\sigma_{ij}/r_{ij})^{12} - (\sigma_{ij}/r_{ij})^6\} + q_i q_j / 4\pi\epsilon_0 r_{ij}$, where r_{ij} is the distance between sites, ϵ_0 is the permittivity of free space, $\sigma_{ij} = (\sigma_i + \sigma_j)/2$, and $\varepsilon_{ij} = (\varepsilon_i \varepsilon_j)^{1/2}$.

these groups were determined by summing the atomic properties of these groups as defined in the early all-atom representation of $[\text{Im}_{41}][\text{PF}_6]$ by Morrow and Maginn.⁵⁶ The bond angle (142°) was chosen to reflect the average disposition of these groups over the conformations adopted by the butyl chain. Because such a simple model was not expected to be capable of accurately reproducing the properties of any real ionic liquid, only an overall scaling of the size parameters σ_i was performed to provide molar volumes close to experimental values of $[\text{Im}_{41}][\text{PF}_6]$.

Molecular dynamics (MD) simulations of the model ionic liquid were performed using a modified version of the DLPOLY_2 code.⁵⁷ Most calculations were done on systems of 343 ion pairs. As a check on whether this size is large enough for the properties of interest here, a much larger system of 2744 ion pairs was also simulated at a single temperature of 450 K. No differences beyond statistical uncertainties were found. Simulations were performed in the NPT ensemble using the Nose-Hoover (Melchionna) algorithms with relaxation times of 0.5 and 2.0 ps for the thermostat and barostat, respectively. Cubic periodic boundary conditions were employed. Rigid body equations of motion were integrated using the Verlet leapfrog integration scheme with a time step of 5 fs. The standard Ewald method with automatic parameter optimization was used to calculate the electrostatic interactions. All nonbonded interactions were calculated within a spherical distance cutoff of 16.0 Å using a Verlet neighbor list with a shell width of 2.0 Å. An initial configuration for these simulations was obtained from an expanded ordered lattice of ion pairs equilibrated first at high temperature which was gradually reduced to 400 K and thereafter equilibrated for 100 ns. Ensembles for other temperatures were derived from this system by further equilibration at the desired temperature (350, 400, 425, 450, 500, and 550 K were studied). All samples were equilibrated for more than 100 ns under the target conditions prior to data collection. Data were collected for a period of 200 ns or more in 5 ns blocks. Block averages were used to estimate statistical uncertainties in the data, which are reported as 2 times the standard deviation of the mean.

Properties determined for purposes of assessing the realism of the model were computed using standard methods.^{58,59} Isothermal compressibilities were computed from fluctuations in the system volume V ,

$$\kappa_T = \frac{\langle (V - \langle V \rangle)^2 \rangle}{k_B T \langle V \rangle} \quad (1)$$

where k_B is Boltzmann’s constant and T the temperature and where the notation $\langle x \rangle$ indicates an average over values of x observed during an equilibrium trajectory. Enthalpies of vapor-

ization were calculated from the average configurational energy E_{liq} of the liquid system of N ion pairs and a gas-phase calculation of a single ion pair E_{gas} via

$$\Delta_{\text{vap}}H(T) = E_{\text{gas}} - E_{\text{liq}}/N + k_{\text{B}}T \quad (2)$$

As suggested by both computational⁶⁰ and experimental⁶¹ studies, volatilization of ionic liquids leads predominantly to gas-phase ion pairs so that these values of $\Delta_{\text{vap}}H$ should be directly comparable to experimental values. Self-diffusion coefficients were calculated from mean square displacements (MSDs) of a given species,

$$\langle r^2(t) \rangle = \frac{1}{N} \sum_{i=1}^N \langle [r_i(0) - r_i(t)]^2 \rangle \quad (3)$$

using the Einstein relation

$$D = \frac{1}{6} \lim_{t \rightarrow \infty} \frac{d}{dt} \langle r^2(t) \rangle \quad (4)$$

Similar procedures were also used to calculate rotational diffusion coefficients of cations as described in section 4. Shear viscosities were calculated by integrating the stress-tensor autocorrelation function,

$$\eta = \frac{V}{k_{\text{B}}T} \int_0^{\infty} \langle P_{\alpha\beta}(0) P_{\alpha\beta}(t) \rangle dt \quad (5)$$

where $P_{\alpha\beta}$ is an off-diagonal element of the stress tensor. Because these correlation functions consisted of a large-amplitude sub-picosecond inertial component and a small-amplitude but slowly decaying diffusive tail, the integration was performed numerically over the first 2 ps and the contribution of the tail estimated by fits to stretched exponential functions. We also calculated viscosities using the Helfand–Einstein approach^{62–64} and obtained comparable results to the Green–Kubo expression, eq 5. However, the former method proved more reliable and was used for the values reported here.

3. Realism of the Model

Figure 2 compares volumetric properties of the model (1 bar) to the experimental data on $[\text{Im}_{41}][\text{PF}_6]$ of Machida et al.⁶⁵ Over the temperature range in which these data overlap, the molar volumes of the model are 1–2% larger than experiment and the isothermal compressibilities (κ_{T}) uniformly smaller than experiment by 16%. The nearly linear changes in the molar volumes with temperature imply average coefficients of thermal expansion of $\alpha_{\text{p}} = 4.4 \times 10^{-4}$ (model) and $5.8 \times 10^{-4} \text{ K}^{-1}$ (experiment) over this range, indicating a 25% underestimation of α_{p} by the model. When considering these and the following comparisons, it should be kept in mind that, while we use $[\text{Im}_{41}][\text{PF}_6]$ for comparison, our main concern is not that the model accurately represent this particular ionic liquid, but rather that its properties be typical of common ionic liquids. In this regard, a recent compilation by Gardas and Coutinho⁶⁶ provides useful perspective. To develop a group contribution method for estimating thermal and transport properties of ionic liquids, these authors compiled experimental values of κ_{T} (22 ILs) and α_{p} (49 ILs) for many combinations of cations and anions in current use. At 1 bar and 298 K average values from these compilations

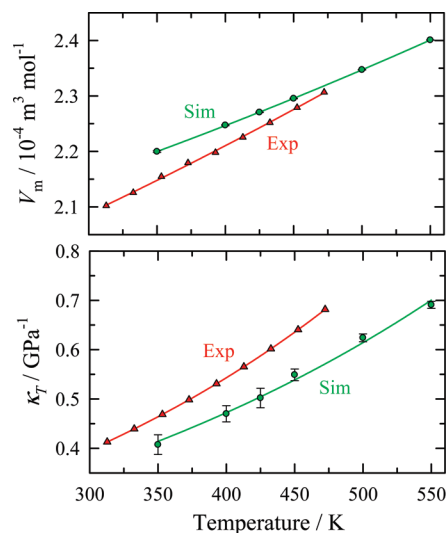


Figure 2. Molar volumes (V_{m}) and isothermal compressibilities (κ_{T}) of the model liquid compared to experimental data on $[\text{Im}_{41}][\text{PF}_6]$.⁶⁵

are $\kappa_{\text{T}} = 0.48 \pm 0.08 \text{ GPa}^{-1}$ and $\alpha_{\text{p}} = (6.2 \pm 0.6) \times 10^{-4} \text{ K}^{-1}$, where \pm here indicates one standard deviation. Although the sensitivity to pressure (i.e., κ_{T}) of the model is smaller than that of $[\text{Im}_{41}][\text{PF}_6]$, its compressibility lies within the range spanned by typical ionic liquids. In contrast, the sensitivity to temperature reflected in α_{p} is significantly lower than is typical. The model value $\alpha_{\text{p}} = 4.4 \times 10^{-4} \text{ K}^{-1}$ lies midway between the values of $(6\text{--}7) \times 10^{-4} \text{ K}^{-1}$ found for most ionic liquids⁶⁶ and the values $(2\text{--}3) \times 10^{-4} \text{ K}^{-1}$ characteristic of alkali halides near their melting points.⁶⁷ As numerous all-atom models of $[\text{Im}_{41}][\text{PF}_6]$ ^{56,21,20,33,30,25,26} predict α_{p} to lie in the range of $(5.2\text{--}7.3) \times 10^{-4} \text{ K}^{-1}$, it seems reasonable to attribute the shortcoming of the idealized model to its lack of intramolecular degrees of freedom.

Structural features are displayed in Figures 3 and 4. In Figure 3 we compare center-of-mass radial distribution functions (rdfs) of the present model to those computed for $[\text{Im}_{41}][\text{PF}_6]$ using all-atom force fields^{56,33,31} and to experimental data on NaCl near its melting point.⁶⁸ At least as far as the rough descriptions of structure afforded by center-of-mass rdfs are concerned, the structure in the present model is similar to that exhibited by all-atom representations. The main difference is that the simpler shape and absence of conformational freedom leads to a sharpening of features in the rdfs of the present model compared to all-atom models. Coordination numbers are similar in the various representations. For example, integrating these rdfs up to the first minimum in the C–A distributions (8.6 or 8.2 Å) yields C–A, C–C, and A–A coordination numbers of 6.8, 7.1, and 6.8 in the present model and 6.2, 6.1, and 6.8 in the all-atom model of Morrow and Maginn.⁵⁶ A more interesting observation is how similar the distributions of all of these room-temperature ionic liquid models are to that of simple inorganic molten salts such as NaCl. This fact is shown in the right-hand panel of Figure 3, where we plot the present model rdfs together with the experimentally determined functions in NaCl at 1148 K⁶⁸ ($T_{\text{f}} = 1081 \text{ K}$). To account for the difference in sizes of the ions in the two liquids, the abscissas of these plots have been scaled to the maximum in $g_{\text{CA}}(r)$. This similarity results from the underlying charge structure common to inorganic molten salts and room-temperature ionic liquids.

The charge structure existing in the IL is better illustrated in Figure 4 (top panel) where all three of the radial distribution

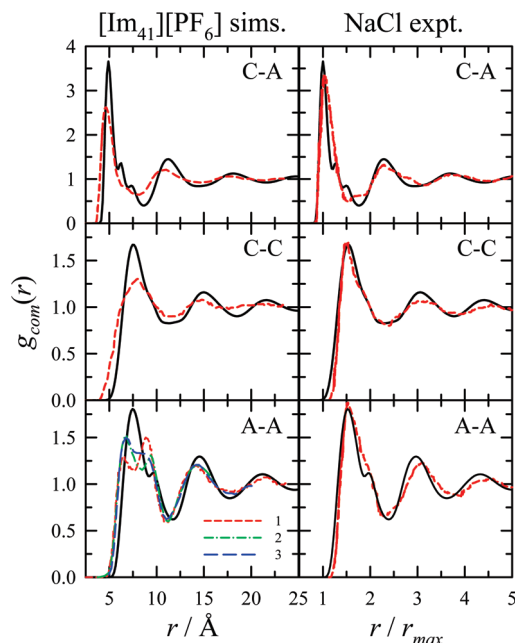


Figure 3. Center of mass radial distribution functions (rdfs) of the model (solid curves) compared to other simulations and experiment. These model rdfs are at 450 K, but there is only a modest change in the features over the range of 350–550 K studied here. The left-hand panel compares the model rdfs to those of the all-atom simulations of [Im₄₁][PF₆] by Morrow and Maginn (no. 1,⁵⁶ red dashed curves) and in the case of the A–A distribution to the simulations of Micaelo et al. (no. 2, green, dashed–dotted curves³³) and Tsuzuki et al. (no. 3, blue long-dashed curves³¹). The right-hand panel compares the simulation model to the experimentally determined rdfs of molten NaCl at 1148 K⁶⁸ (red dashed curves). For comparison the distance scales have been normalized by the position of the first peak of $g_{CA}(r)$, r_{max} .

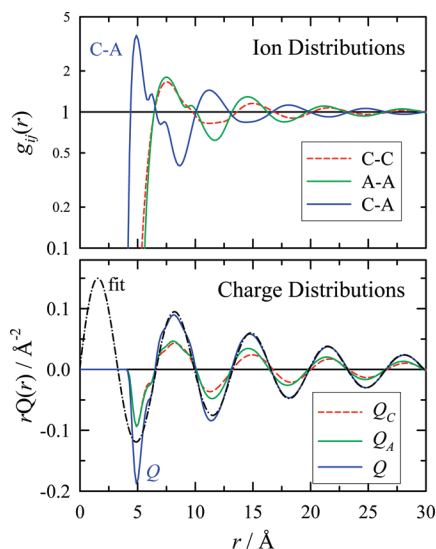


Figure 4. Center of mass radial distribution functions (g_{ij} , top) and charge distribution functions ($Q(r)$ bottom) calculated from them. The dashed–dotted curve in the lower panel is a fit of the total charge distribution function to eq 6 with parameters $A = 0.17 e \text{ \AA}^{-2}$, $d = 6.6 \text{ \AA}$, $\varphi = 0$, and $\lambda = 14.5 \text{ \AA}$.

functions are plotted together in order to emphasize the marked alternation of charge that is present. The bottom panel examines this structure more directly using charge distribution functions, $Q_i(r)$, defined such that $4\pi r^2 q_i Q_i(r) dr$ is the net charge at a distance r from a central ion i of charge q_i .⁶⁹ These functions are related to the radial distribution functions by $Q_C(r) = \rho[g_{CC}(r) - g_{CA}(r)]$, $Q_A(r) = \rho[g_{AA}(r) - g_{CA}(r)]$, and $Q(r) =$

$Q_C(r) + Q_A(r)$,⁷⁰ where ρ is the ion density ($\rho_C + \rho_A$). The (total) charge distribution function $Q(r)$ provides a convenient overall description of charge ordering in systems comprised of comparably sized cations and anions. As reviewed by Koblinski et al.,⁶⁹ theories of ionic liquids and solutions suggest that at high ionic strengths (small Debye–Hückel screening lengths) $Q(r)$ should approach the general form

$$Q(r) = \frac{A}{r} \exp(-r/\lambda) \sin\{2\pi r/d + \varphi\} \quad (6)$$

at separations larger than the first few solvation shells. As demonstrated by the curve labeled “fit” in Figure 4, this function closely fits the decay of $Q(r)$ after the first full (cation + anion) solvation shell, with fit parameters $A = 0.17 e \text{ \AA}^{-2}$, $d = 6.6 \text{ \AA}$, $\varphi = 0$, and $\lambda = 14.5 \text{ \AA}$. It is instructive to compare this charge structure with that found in molten NaCl, which has been simulated over a broad range of thermodynamic conditions.⁶⁹ To account for the difference in ion sizes, we rewrite the above parameters in terms of an effective C–A pair distance σ (5.4 \AA), which produces the following: $A = 4.9 e \sigma^{-2}$, $d = 1.2 \sigma$, and $\lambda = 2.7 \sigma$. Comparable values for NaCl near its melting point (1081 K) are then $A \cong 5 \sigma^2$, $d \cong 1.3 \sigma$, $\varphi \cong 0$, and $\lambda \cong 2.3 \sigma$. Thus, the charge structuring that occurs in this ionic liquid model is indeed quite similar to that of an alkali halide melt. The structure is relatively long-ranged, having a decay constant λ the size of two to three solvation shells, which implies substantial coupling (interactions $> 5k_B T$) among collections of > 100 ions.⁷¹ To our knowledge, the only other study to fit $Q(r)$ in an ionic liquid in this manner was an early study of [Im₂₁][NO₃] by Del Pópolo and Voth.⁷² These authors estimated a value $\lambda = 7 \text{ \AA}$ ($\sim 1.5 \sigma$), considerably smaller than found here. It is possible that the fact that a smaller system size (216 versus 2744 or 343 ion pairs here) was employed in the former work contributes to this smaller correlation length, but it is also likely that the simpler shape of the ions in the present study leads to a more readily observable and coherent charge structure, more like that of NaCl. Nevertheless, the underlying balance of electrostatic interactions and strong coupling among large collections of ions implied by this structure should be a general feature of room-temperature ionic liquids.

Some energetic properties of the model liquid are listed in Table 2. E_{el} and E_{LJ} are the electrostatic and Lennard-Jones contributions to the internal energy of the liquid and $\Delta_{vap}H$ is the enthalpy of vaporization calculated assuming that the vapor phase consists entirely of ion pairs.^{61,73} The value of $\Delta_{vap}H$ extrapolated to 298 K is $210 \pm 5 \text{ kJ/mol}$. This value can be compared to values obtained from realistic simulation models of [Im₄₁][PF₆],^{56,20,74,33,25,26} which range between 123³³ and 190 kJ/mol.⁷⁴ $\Delta_{vap}H$ has not been directly measured for [Im₄₁][PF₆], but a reasonable estimate based on two recent studies^{75,76} is $162 \pm 10 \text{ kJ/mol}$ at 298 K. The value of $\Delta_{vap}H$ of our idealized model is about 30% larger than the experimental estimate. More importantly, the value of 210 kJ/mol is larger than all of the vaporization enthalpies listed in a recent compilation of experimental results for 20 ionic liquids,⁷⁶ where the largest value is 190 kJ/mol. This overestimation of $\Delta_{vap}H$ does not necessarily mean that the model liquid is too strongly bound because $\Delta_{vap}H$ reflects the *difference* between two larger energies—the energy of the liquid relative to the energy of the ion pairs that make up the gas phase. (It is for this reason that alkali halides near their melting points exhibit values of $\Delta_{vap}H = 140\text{--}210 \text{ kJ/mol}$,⁷⁷ comparable to the values found for room-temperature ionic liquids, despite the much higher liquid-phase

TABLE 2: Calculated Properties^a

	<i>T</i> /K	<i>V_m</i> /(10 ⁻⁴ m ³ mol ⁻¹)	<i>κ_T</i> /GPa ⁻¹	- <i>E_{el}</i> /(kJ mol ⁻¹)	- <i>E_{LJ}</i> /(kJ mol ⁻¹)	<i>Δ_{vap}H</i> /(kJ mol ⁻¹)	<i>D_C</i> /(10 ⁻¹² m ² s ⁻¹)	<i>D_A</i> /(10 ⁻¹² m ² s ⁻¹)	<i>η</i> /(mPa s)
ionic liquid	350	2.200	0.41	415	53	207	[0.9]	[0.4]	[27500]
	400	2.247	0.47	412	51	198	9(2)	6(2)	659(54)
	425	2.271	0.50	410	50	196	24(2)	16(3)	253(48)
	450	2.295	0.55	409	49	190	54(5)	40(5)	83(11)
	500	2.347	0.62	406	47	187	167(10)	140(12)	22(4)
	550	2.401	0.69	403	46	186	380(25)	350(30)	9.1(2)
neutral mixture (NM)	298	2.70	1.62	0	57	59	2.3 × 10 ³	2.6 × 10 ³	0.38

^a *V_m* and *κ_T* denote molar volume and isothermal compressibility, *E_{el}* and *E_{LJ}* are the electrostatic and Lennard-Jones contributions to the internal energy, and *Δ_{vap}H* is the enthalpy of vaporization. Calculations of *Δ_{vap}H* assumed the gas phase to consist of purely ion pairs in the case of the IL and of fully dissociated species in the case of the NM. Uncertainties in these values are <2 in the final digit. *D₊* and *D₋* are translational diffusion coefficients of the cation and anion, and *η* is the shear viscosity. Uncertainties in the final digits are indicated in parentheses; brackets indicate highly uncertain values. The “neutral mixture” data (discussed in section 5) are from *NPT* simulations in which all charges are removed from the IL model.

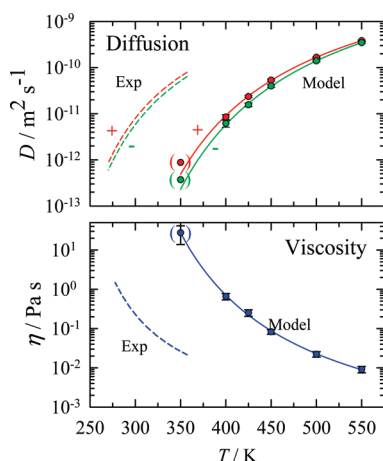


Figure 5. Diffusion coefficients and shear viscosity of the model compared to experimental data on [Im₄₁][PF₆]. Experimental curves (dashed) are from the parametrizations of Tokuda et al.⁷⁹ The curves drawn through the simulated data are fits to the functional form $Y = Y_0 \exp \{B/(T - T_0)\}$ with the following parameters given in the format $Y = \{Y_0, B/K, T_0/K\}$: cation diffusion $D_C = \{5.30 \times 10^{-8} \text{ m}^2 \text{ s}^{-1}, -1715, 202\}$, $D_A = \{7.67 \times 10^{-8} \text{ m}^2 \text{ s}^{-1}, -1877, 202\}$, and viscosity $\eta = \{4.42 \times 10^{-5} \text{ Pa s}, 1765, 218\}$. Data points in parentheses are highly uncertain and were not used in the fits.

binding energies in the alkali halides.) The liquid-phase energies *E_{el}* and *E_{LJ}* are typical of values found in more realistic representations of [Im₄₁][PF₆]^{19,20,74} and related ionic liquids.^{27,78} The reason that *Δ_{vap}H* is too large in the idealized model is that binding of the gas-phase ion pair (~270 kJ/mol) is too small relative to the energy of the liquid. Apparently, the idealized model lacks the conformational flexibility and the complex shape and charge distribution that enables more sophisticated models to achieve more stable gas-phase ion-pair structures and thereby more realistic values of *Δ_{vap}H*.

Finally, in Figure 5 we compare dynamics of the model to experiment, using as experimental benchmarks the self-diffusion coefficients (*D_C*, *D_A*) and viscosity (*η*) of [Im₄₁][PF₆] measured by Watanabe and co-workers.⁷⁹ As illustrated here, the direct correspondence between the model and experimental transport properties is poor. For example, at 350 K, the model diffusion coefficients are roughly 100-fold smaller than experimental values. This shortcoming is not surprising given the simplicity of the model. Recent work of Lynden-Bell and Youngs³² has shown that even with an all-atom representation of [Im₁₁][Cl], simplifications of the cation charge distribution similar to those made here lead to reductions in the cation and anion diffusion coefficients of between 10- and 30-fold. Moreover, as illustrated by Figure S1 (Supporting Information), even all-atom models

of [Im₄₁][PF₆] have difficulty in reproducing these dynamical properties accurately. There are, however, obvious similarities between the model and experimental transport properties. To a good first approximation, the values of *D_C*, *D_A*, and *η* of the idealized model map onto those measured experimentally for [Im₄₁][PF₆] at a 100–110 K lower temperature. In studies of solvation to be reported later, we also find that a ~100 K temperature shift brings dynamic Stokes shifts simulated using this model into line with experimental measurements in [Im₄₁][PF₆]. Thus, it seems reasonable to use the present model to represent generic features of ionic liquid behavior simply by accounting for this 100 K shift when making comparison to experimental dynamics. Interestingly, Tsuzuki et al.³¹ recently reported that a similar shift of ~100 K is required to achieve correspondence between the predictions of their all-atom force field and the measured diffusion coefficients of 13 common ionic liquids.

4. Characterizing Ion Dynamics

As a first characterization of the dynamics of the model, we examine mean squared displacements in Figure 6. The top panel of Figure 6 shows translational displacements (MSDs) of cation centers of mass at five temperatures in the range of 350–550 K. These MSDs exhibit features characteristic of supercooled liquids,⁸⁰ as has already been noted in prior simulations of ionic liquids.^{81,72,82} Three time regimes of ion translation are clearly delineated at the lower temperatures: a ballistic regime at early times (<1 ps here) wherein $\langle r^2 \rangle$ increases quadratically with time, a diffusive regime at long times (>100 ps) where $\langle r^2 \rangle$ increases linearly with time, and a subdiffusive regime at intermediate times where $\langle r^2 \rangle \propto t^p$ with $p < 1$. The subdiffusive or plateau region in these log–log plots indicates times over which ions remain trapped within the confines of the local cage formed by their neighbors, before there has been significant reorganization of local environments. It is the presence of this last regime, which is absent in normal liquids, that is characteristic of systems approaching a glass transition. In the present model liquid the subdiffusive regime begins before 1 ps at all temperatures, but its extent varies markedly with temperature. It ends when $\langle r^2 \rangle \sim 30 \text{ Å}^2$ or when the root-mean-squared (rms) displacement of ions is about one ion diameter (5–6 Å). This time is ~100 ps at 550 K, ~1 ns at 450 K, and >10 ns at 350 K. At this lowest temperature, structural relaxation is sufficiently slow that our simulations fail to adequately sample many dynamical properties. (Simulations of cooling, shown in Figure S2 of the Supporting Information, indicate that below ~325 K the system cannot achieve equilibrium on the simulation time scale, suggesting a glass transition near to but below this

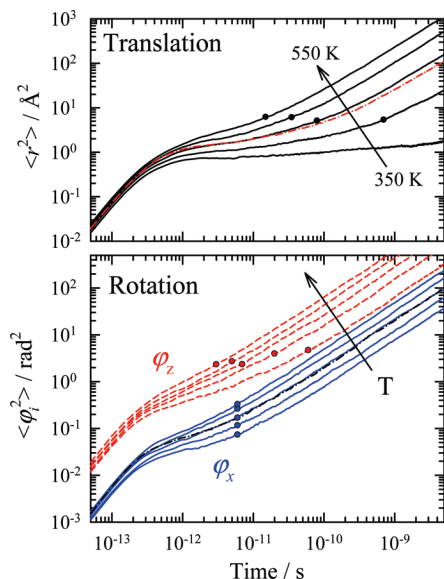


Figure 6. Mean squared displacements (MSDs) at 350, 400, 450, 500, and 550 K. The top panel shows translational MSDs of the cations (solid curves). The red dashed-dotted curve in this panel is the anion displacement at 450 K. The bottom panel shows orientational MSDs corresponding to rotations about the x and z inertial axes. The dashed-dotted curve in this panel is the ϕ_y MSD at 450 K. The filled symbols denote the approximate positions of the maximum in the non-Gaussian parameter shown in Figure 10.

temperature.) The red dashed curve in the top panel of Figure 6 shows $\langle r^2 \rangle$ of the anions at 450 K. At this temperature, and at all other temperatures, anion and cation displacements are very similar. The close correspondence between anion and cation MSDs and diffusion coefficients, also noted in many previous simulations and experiments,^{82,31,83} highlights the coupled nature of cation and anion translations in ionic liquids.

The equivalent of $\langle r^2 \rangle$ for orientational motions of the polyatomic cations is shown on the bottom panel of Figure 6. These $\langle \phi_i^2 \rangle$ are computed by integrating body-fixed angular velocities ω_i ,⁸⁴ $\phi_i(t) = \int_0^t \omega_i(t') dt'$, where $i = x, y$, or z denotes a principal axis direction. (See Figure 1 for axis definitions.) Use of integrated velocities in this manner makes the $\phi_i(t)$ unbounded, which enables calculation of rotational diffusion coefficients about each axis using an Einstein relation similar to that for translation.⁸⁴

$$D_{r,i} = \frac{1}{2} \lim_{t \rightarrow \infty} \frac{d}{dt} \langle \phi_i^2(t) \rangle \quad (7)$$

For brevity, in Figure 6 and later figures, we only show results for the x and z inertial axes because $\langle \phi_i^2 \rangle$ as well as the orientational correlation functions discussed later are nearly identical for $i = x$ and y . As can be seen from Figure 6, subdiffusive dynamics are also present in the case of rotation, but they are less pronounced than in the translational case. The ballistic regime again ends before 1 ps, but for rotations the onset of diffusive dynamics (i.e., $\langle \phi^2 \rangle \propto t^1$) occurs sooner than for translation. For example, at 450 K, although the extent of motion $\langle \phi_i^2 \rangle$ differs between ϕ_x ($\sim \phi_y$) and ϕ_z due to the 10-fold difference in moments of inertia (I_x, I_y , and $I_z = 646, 585$, and $61 \text{ m}_u \text{ \AA}^2$, respectively) the onset of diffusive displacements occurs near 100 ps for all rotation axes, whereas it occurs near 1 ns for translation. At this temperature, in the time that it takes for the rms displacement to equal one ionic diameter, cations have progressed by average rotation angles of $\sim 250^\circ$ in ϕ_x and

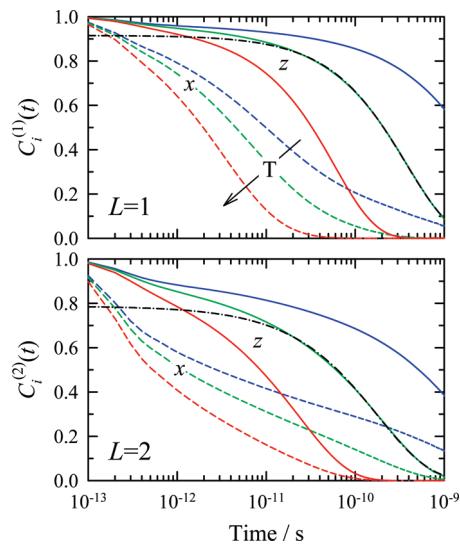


Figure 7. First (top) and second (bottom) rank orientational correlation functions (eq 8) of unit vectors along the x and z inertial axes at temperatures of 400, 450, and 550 K. The dashed-dotted curves in both panels are stretched exponential fits to the 450 K z -axis correlation functions.

ϕ_y and 540° in ϕ_z . At lower temperatures, angular displacements are even larger during the time when translations are showing caged dynamics. Thus, appreciable rotation can occur without significant structural reorganization.

A different perspective on rotational dynamics is provided by the reorientational time correlation functions

$$C_i^{(L)}(t) = \langle P_L[\hat{u}_i(0) \cdot \hat{u}_i(t)] \rangle \quad (8)$$

where \hat{u}_i denotes a unit vector along one of the inertial axes i and P_L is the Legendre polynomial of order L . Here we consider only $P_1(x) = x$ and $P_2(x) = (3/2)x^2 - (1/2)$. Representative correlation functions are shown in Figure 7. In comparing these correlation functions to the data in Figure 6, one must keep in mind the fact that $\langle \phi_i^2(t) \rangle$ measures rotation about axis i , whereas $C_i^{(L)}(t)$ measures rotation of axis i . Thus, $C_z^{(L)}(t)$ depends only on rotations about the x and y inertial axes, i.e., on $\theta_x(t)$ and $\theta_y(t)$, and is unaffected by θ_z rotations. Because the moments of inertia and dynamics of $\theta_x(t)$ and $\theta_y(t)$ are similar, $C_z^{(L)}(t)$, which describes reorientation of the long molecular axis is the simplest of the correlation functions. It describes a nearly “pure” rotational motion similar to what would be found for reorientation of a linear molecule. (The cation dipole moment referenced to the center of mass lies within 6° of the z axis, also making $C_z^{(L)}(t)$ the function relevant to the dielectric response.) In contrast, the time dependence of $C_x^{(L)}(t)$ and $C_y^{(L)}(t)$ are more complex because these functions are effected by rotations about two axes, y or x and z , whose moments of inertia and diffusion rates differ greatly. As shown in Figure 7, both types of correlation function have at least two components: a typically small inertial component confined to sub-picosecond times, followed then by a dominant component on the picosecond to nanosecond time scales which accounts for 70–95% of the relaxation. Beyond 1 ps the $C_z^{(L)}(t)$ correlation functions can be well-fit by a stretched exponential time dependence (dashed-dotted curves) with stretching exponents β in the range of 0.75–0.85, with $\beta(L=1) > \beta(L=2)$. The $C_x^{(L)}(t)$ functions are much more broadly distributed in time and require at least two exponentials to achieve a reasonable fit. Furthermore, whereas

the correlation times of $C_z^{(1)}(t)$ and $C_z^{(2)}(t)$ are approximately in the ratio of 3:1 expected for a diffusive process, $C_x^{(1)}(t)$ and $C_x^{(2)}(t)$ cross on a picosecond time scale such that the correlation times of the $L = 2$ function are actually larger than those of $L = 1$. The same observations apply to $C_y^{(L)}(t)$. Similar crossing of the $L = 1$ and $L = 2$ functions was found by Shim and Kim for a diatomic solute⁸⁵ and for the cations in their united atom [Im₂₁][PF₆] model⁴³ as well as in an early study of rotational dynamics of a model glass-forming diatomic liquid.⁸⁶ In both cases this crossover was attributed to the fact that large-angle jumps contribute importantly to the correlation functions, which will also be shown to be the case here.

Before discussing the nature of the translational and rotational motions in more detail, we digress in order to discuss the behavior expected on the basis of simple hydrodynamic models of the sort often used to interpret experimental data. Such models assume that friction is proportional to viscosity and predict times (or rates) which are proportional (or inversely proportional) to η/T . If one assumes molecules to be spherical in shape and to have radius R and volume V , the hydrodynamic predictions are simply

$$D_{\text{trans}} = \frac{k_B T}{\eta R} f_{\text{BC}} \quad f_{\text{stick}} = \frac{1}{6\pi}, \quad f_{\text{slip}} = \frac{1}{4\pi} \quad (9)$$

$$D_{\text{rot}} = \frac{k_B T}{\eta V} f_{\text{BC}} \quad f_{\text{stick}} = 1, \quad f_{\text{slip}} = \infty \quad (10)$$

where f_{BC} is a factor dependent on the boundary condition assumed for motion of the surrounding continuum fluid tangential to the surface of the sphere (stick or slip). For a spherical object, all axes are equivalent and $C^{(L)}(t)$ decays exponentially with time constant

$$\tau_{\text{rot}}^{(L)} = [L(L+1)D_{\text{rot}}]^{-1} \quad (11)$$

Equations 9–11 are appropriate for PF₆[−], especially for the single-site representation used here. For more complicated objects such as the cation, the same proportionalities to η/T apply but with different boundary-condition-dependent factors f_{BC} for each principal axis i . To obtain explicit hydrodynamic predictions, we approximate the cation as an ellipsoid, a shape for which values of f_{BC} can be determined or are available in the literature. Details of how these factors are obtained can be found elsewhere.⁸⁷ Independent of these factors, if motion can be described as small-step diffusion, the following relationships should hold between the three principal components of the rotational diffusion tensor $\{D_i\}$ and the rotational correlation functions $C_j^{(L)}(t)$ ($i, j = x, y, z$).^{88,89}

$$C_i^{(1)}(t) = \exp\{-(3D_{\text{rot}} - D_i)t\} \quad (12)$$

$$C_i^{(2)}(t) = \left(\frac{1}{2} + \frac{3(D_{\text{rot}} - D_i)}{4\Delta}\right) \exp\{-(6D_{\text{rot}} + 2\Delta)t\} + \left(\frac{1}{2} - \frac{3(D_{\text{rot}} - D_i)}{4\Delta}\right) \exp\{-(6D_{\text{rot}} - 2\Delta)t\} \quad (13)$$

where

$$D_{\text{rot}} = \frac{1}{3}(D_x + D_y + D_z) \quad \text{and} \quad \Delta = \sqrt{D_x^2 + D_y^2 + D_z^2 - D_x D_y - D_x D_z - D_y D_z} \quad (14)$$

In contrast to the spherical case, rotation of an axis i includes contributions from the two other axes D_j and D_k ($j, k \neq i$) making $C_i^{(L)}(t)$ generally multiexponential, a fact which typically spoils any simple relationship between correlation times of different order (such as $\tau^{(1)} = 3\tau^{(2)}$ implied by eq 11).

Returning now to the present system, Figures 8 and 9 illustrate how the translational diffusion coefficients D_C and D_A , the rotational correlation times $\tau_i^{(L)}(i = x, z)$, and diffusion coefficients D_i of the cation ($i = x, y, z$) vary with η/T . As shown in Figure 8, both translational diffusion coefficients and rotational correlation times are approximately proportional to η/T , as anticipated by hydrodynamic models. Over the 200 K temperature range studied, all of these data are reasonably represented by power-law relationships of the form $A = A_0(\eta/T)^p$ with powers $0.8 \leq |p| \leq 1.0$. This sort of power law is common,^{90,91} and such departure from the hydrodynamic expectation $|p| = 1$ is probably best viewed as resulting from changes in the strength of the coupling between the diffuser and its surroundings with temperature.⁹²

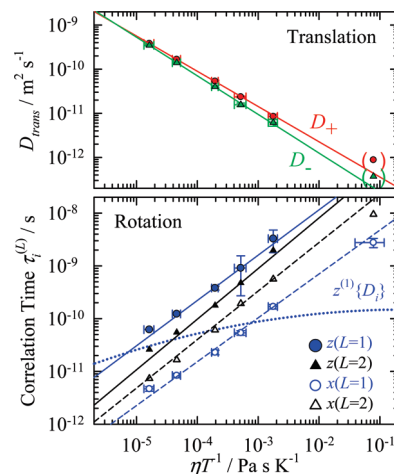


Figure 8. Translational diffusion coefficients (top) and rotational correlation times (bottom) plotted versus η/T . The lines are power-law fits of the form $A = A_0(\eta/T)^p$ resulting in the following powers: (D_C , D_A , $\tau_z^{(1)}$, $\tau_z^{(2)}$, $\tau_x^{(1)}$, $\tau_x^{(2)}$) = (−0.79, −0.88, 0.86, 0.96, 0.83, 0.92). The dashed–dotted curve labeled “ $z^{(1)}\{D_i\}$ ” is the correlation time of $C_z^{(1)}(t)$ calculated using fitted values of the rotational diffusion coefficients in eqs 12–14.

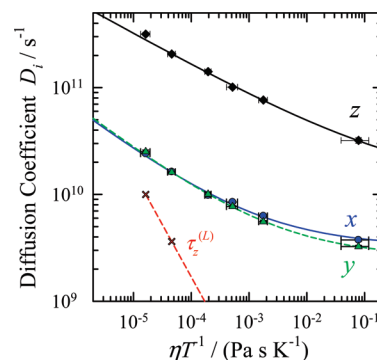


Figure 9. Rotational diffusion coefficients calculated according to eq 7. The dashed line labeled $\tau_z^{(L)}$ represents the average of the x , y diffusion coefficients estimated from the first and second rank z -axis correlation times using the relation $D = [L(L+1)\tau^{(L)}]^{-1}$.

TABLE 3: Comparison to Hydrodynamic Predictions at 450 K^a

motion	quantity	ionic liquid			neutral mixture		
		value	slip ratio	stick ratio	value	slip ratio	stick ratio
Translational Diffusion Coefficients							
anion	$D_A/(10^{-11} \text{ m}^2 \text{ s}^{-1})$	4.0	1.5	2.3	170	1.0	2.1
cation	$D_C/(10^{-11} \text{ m}^2 \text{ s}^{-1})$	5.4	1.6	2.3	150	0.7	1.4
Cation Rotational Correlation Times							
rotation of x	$\tau_x^{(1)}/\text{ps}$	27	20	222	2.6	2.9	31
rotation of x	$\tau_x^{(2)}/\text{ps}$	66	4.1	31	2.3	1.6	12
rotation of y	$\tau_y^{(1)}/\text{ps}$	27	18	230	2.6	2.5	32
rotation of y	$\tau_y^{(2)}/\text{ps}$	51	4.4	41	2.1	1.4	13
rotation of z	$\tau_z^{(1)}/\text{ps}$	440	3.9	19	20	1.2	5.8
rotation of z	$\tau_z^{(2)}/\text{ps}$	220	2.7	13	6.6	1.2	5.8
Cation Rotational Diffusion Coefficients							
rotation about x	$D_x/(10^{10} \text{ s}^{-1})$	1.1	26	180	3.4	1.1	8
rotation about y	$D_y/(10^{10} \text{ s}^{-1})$	1.0	55	160	3.2	2.4	7.1
rotation about z	$D_z/(10^{10} \text{ s}^{-1})$	14	83	1300	40	3.3	52

^a Values of observed quantities are provided in the columns labeled “value”, which are from temperature-dependent fits of the sort shown in Figures 8 and 9. Uncertainties in these quantities are less than 10%. The viscosities used for calculation are 83 mPa s in the ionic liquid and 1.15 mPa s in the neutral mixture (see section 5). Hydrodynamic predictions⁸⁷ are provided as ratios of observed to predicted rates; i.e., the ratios are of observed/predicted quantities in the case of diffusion coefficients and predicted/observed quantities in the case of rotation times. The anion was modeled as a sphere of radius $R = 2.61 \text{ \AA}$. For calculating translational diffusion coefficients the cation was modeled as a prolate ellipsoid with semiaxes $(a, b, b) = (5.00, 2.56, 2.56) \text{ \AA}$. For calculating rotational characteristics of the cation, an asymmetric ellipsoid with semiaxis dimensions $(a, b, c) = (5.00, 3.00, 2.18) \text{ \AA}$ was used. In all cases the volume of the approximating object was matched to the volume determined by the Lennard-Jones σ parameters of the model.

Interestingly, the rotational diffusion coefficients, shown in Figure 9, behave quite differently from the former quantities. Over the temperature range studied here a power law does not adequately capture these data. Rather than being constant and near unity, the slopes of the curves, $p = d \ln(D_i)/d \ln(\eta/T)$, are at all temperatures much smaller and appear to approach $p = 0$ at low temperatures. Thus, in contrast to D_{trans} and τ_{rot} , which remain tied to viscosity over the range studied, the rotational diffusion coefficients D_i appear to decouple from viscosity, i.e., from the structural relaxation of the liquid, as temperature is lowered. Given that the rotational diffusion coefficients and correlation times are merely different measures of the same molecular motions, their qualitatively different temperature dependence is initially puzzling. For example, if the limit of small-step diffusion is applicable, these two quantities are directly interrelated by eqs 12–14. In this limit the $\tau_i^{(L)}$ can be calculated from the $\{D_i\}$. The dotted curve in Figure 8 labeled “ $\tau_z^{(1)}\{D_i\}$ ” illustrates this connection for the case of $\tau_z^{(1)}$, the correlation time of the first rank correlation function for rotation of the long molecular axis. Although the values of $\tau_z^{(1)}$ calculated from the D_i appear to approach the observed correlation times at the higher temperatures, even at the upper limit of the simulated temperature range the calculated times are about 6-fold smaller than observed. (The dashed curve in Figure 9 labeled “ $\tau_z^{(L)}$ ” is an approximate calculation of $D_x \cong D_y$ from $\tau_z^{(1)}$ and $\tau_z^{(2)}$, which shows the same result.)

Clearly, description of these data in terms of small-step diffusion is inappropriate for this system. To the best of our knowledge, comparisons of this type are rare. But in a recent report by Lombardo et al.⁸⁴ very similar behavior was reported for a three-site model of *o*-terphenyl in the supercooled liquid region. These authors emphasized how the distinct temperature dependencies of τ_{rot} and D_{rot} , such as those displayed in Figures 8 and 9 might require reinterpretation of experimental results on translation–rotation coupling in deeply supercooled liquids.⁹³ In the *o*-terphenyl case, failure of the expected connection between τ_{rot} and D_{rot} was attributed to large-angle jumps becoming important in the supercooled regime. As we will discuss shortly, the same mechanism is also operative here.

To conclude discussion of hydrodynamic models, Table 3 provides comparisons of observed translation and rotation rates or times at 450 K to hydrodynamic predictions using spherical anion and ellipsoidal cation approximations. (In addition to results for the model ionic liquid, Table 3 also presents analogous results on a neutral mixture to be discussed in the following section.) The temperature 450 K lies in the middle of the range studied, and the comparisons provided here are representative of what is found at all temperatures except the lowest. The columns labeled “slip ratio” and “stick ratio” in this table are ratios of observed rates to those calculated from hydrodynamics using these two boundary conditions. Note that irrespective of whether the quantity considered is a diffusion coefficient or a rotation time the ratio is reported such that a value greater than one indicates faster observed dynamics than predicted by hydrodynamic estimates.

In the case of translational diffusion, the predictions of slip and stick calculations do not differ greatly, and either calculation provides reasonable estimates of the observed D_A and D_C . These results are consistent with experimental measurements of temperature-dependent cation and anion diffusion coefficients in a variety of ionic liquids by Watanabe and co-workers, which can generally be predicted to within a factor of 2 using slip calculations and spherical ion representations.^{79,94,95,83} In the case of rotation, slip and stick predictions differ more significantly. Here stick predictions are clearly too slow, at least 10 times slower than the simulated rotational dynamics. Slip calculations provide closer estimates of the observed dynamics, but even here the predictions are at least 3-fold slower than observed. Finally, Table 3 shows that even the slip calculations predict rotational diffusion coefficients more than 20 times smaller than observed values. This failure is expected given the previous discussion of the failure of eqs 12–14 to relate the $\tau_i^{(L)}$ and $\{D_i\}$.

We now consider some details of the molecular motions responsible for the behavior of these various observables. The first aspect of interest is dynamic heterogeneity, the presence of varying rates of motion for different molecules or subensembles. It is common to associate heterogeneity of translational

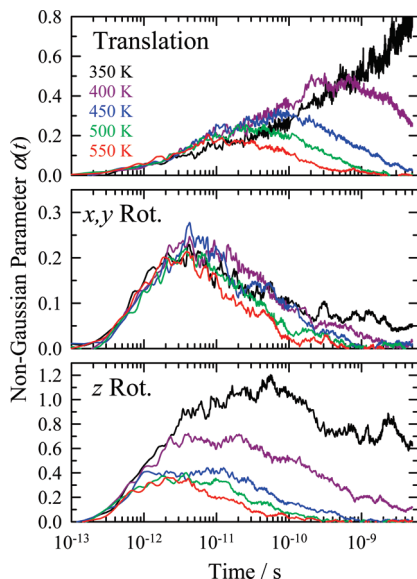


Figure 10. Time evolution of the non-Gaussian parameter α (eq 15) calculated from translational and rotational mean squared displacements of cations. The results for rotation about the x and y axes are similar, and averages over these two axes are shown in the middle panel.

motions with the non-Gaussian character of the self van Hove function describing the time-dependent probability distribution of translational displacements.^{96,84,72,97,98,82} For a purely diffusive process in a single dimension x , displacements should be Gaussian in Δx at all times, and departure from this expectation can be monitored using the parameter^{99,84}

$$\alpha(t) = \frac{1}{5} \frac{\langle \Delta x(t)^4 \rangle}{\langle \Delta x(t)^2 \rangle^2} - \frac{3}{5} \quad (15)$$

As discussed by Lombardo et al.,⁸⁴ this non-Gaussian parameter is equally applicable to both translational and rotational MSDs of the sort examined here. It is for this reason we report one-dimensional displacements for translation in contrast to the more usual practice of reporting the equivalent parameter for three-dimensional displacements, $\alpha = 3 \langle \Delta r^4 \rangle / 5 - 1$.^{100,99} However, the definition of α in eq 15 is scaled such that the two values should be identical in isotropic systems.

Figure 10 shows the non-Gaussian parameters observed as functions of temperature. In the case of translation, $\alpha_{\text{trans}}(t)$ exhibits a maximum whose amplitude increases and whose location shifts to longer times with decreasing temperature. As indicated in Figure 6, the location of maximal non-Gaussian character occurs near the end of the subdiffusive region but before the MSDs become simply proportional to time. At 400 and 450 K, temperatures where we expect the model to be comparable to experimental systems, $\alpha_{\text{trans}}(t)$ reaches maximal values of 0.3–0.5 at times of 100 ps to 1 ns. This behavior is comparable to what has been observed in all-atom simulations of ionic liquids by several workers.^{72,98,82} Hu and Margulis,⁹⁷ who simulated $[\text{Im}_{41}][\text{PF}_6]$, found larger values: $\alpha_{\text{trans}} \sim 0.7$ (100 ps) at 400 K and 1.35 (2 ns) at 300 K. In the case of rotations, the non-Gaussian parameter measured for rotation about the long molecular axis, $\alpha_{z,\text{rot}}(t)$, behaves similarly to $\alpha_{\text{trans}}(t)$ but with slightly larger maximum values occurring at shorter times. MSDs for rotation about the other two axes x and y are much closer to Gaussian in character, with values of $\alpha_{x/y,\text{rot}}$ remaining below 0.25. In addition, the $\alpha_{x/y,\text{rot}}(t)$ are largely temperature-independent. Although comparable rotational results do not exist

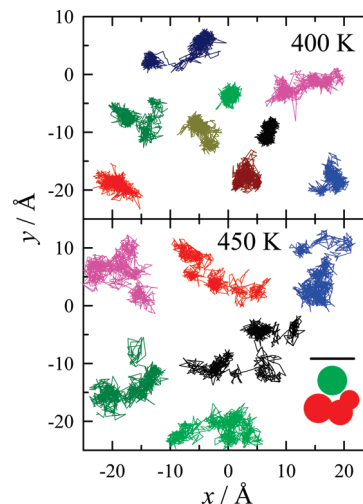


Figure 11. Two-dimensional projections of 5 ns trajectories of the centers of mass of selected cations at 400 and 450 K. For reference, the diagram at the lower right indicates the sizes of the cation (red) and anion (green) and the bar the distance of the first peak in the cation–cation radial distribution function. Note that no information concerning the spatial correlations between dynamics of different ions should be inferred from these plots because of the absence of the third dimension and because some ions have been moved for clarity.

for other ionic liquids, our observations are remarkably close to those made by Lombardo et al. in their simulations of an idealized model of *o*-terphenyl in the deeply supercooled region.⁸⁴

A visual sense of the nature of translational motions is provided in Figure 11, where we plot representative 5 ns trajectories of cation centers of mass at 400 and 450 K. Anion trajectories are similar. The main observation to be made from plots such as these is that translational movement occurs both from ions rattling within the cage formed by their neighbors and continuously deforming this cage, together with intermittent large-amplitude jumps of length comparable to an average cation–cation separation. The jump motions are probably partially responsible for translations not obeying Gaussian statistics (i.e., $\alpha_{\text{trans}} > 0$), but dynamic heterogeneity, clearly visible in the 400 K plots, is the primary origin of the behavior shown in Figure 10. Although we did not pursue further analysis here, prior work indicates that fast- and slow-moving molecules are spatially correlated^{72,97,93} and that the rate of rotation of a molecule is not necessarily correlated with its translational mobility.^{97,84}

Figures 12 and 13 further analyze the rotational motion of the cations in this system and help explain why the rotation rates reported by MSDs and correlation times depart so dramatically from small-step diffusion expectations at low temperatures. In Figure 12 we show how the orientations of the x (or y) and z molecular axes evolve in time, using the distribution function⁸⁵

$$G_i(\theta, t) = \langle \delta \{ \cos^{-1} [\hat{u}_i(0) \cdot \hat{u}_i(t)] - \theta \} \rangle \quad (16)$$

Note that here we are focusing on rotation of the molecular axes, whereas the non-Gaussian parameters associated with rotational motion in Figure 9 derive from characteristics of analogous distributions of angular displacements (the φ_i) about the molecular axes. The $G_i(\theta, t)$ are much more informative in the present system. The top panel of Figure 11 shows that that time evolution of the long molecular axis, $G_z(\theta, t)$, is roughly

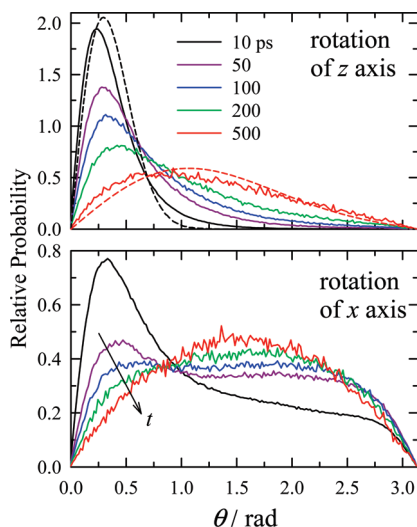


Figure 12. Orientation distributions $G_i(\theta, t)$ at 450 K for rotation of the z and x molecular axes at the times indicated. The y -axis distributions are nearly indistinguishable from the x -axis distributions and are not shown. The dashed curves in the upper panel are best fits of the 10 and 500 ps distributions to the form expected for simple diffusive rotation.

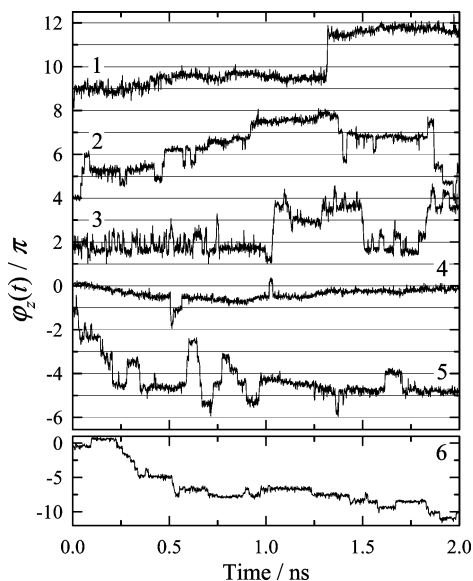


Figure 13. Trajectories of angular displacements about the z axis at 350 K for six selected cations. The top panel shows typical trajectories of five cations selected at random, whereas the bottom panel contains a less common trajectory of an ion having a large net displacement. All ion trajectories begin at $\varphi_z(0) = n\pi$.

what is expected for simple diffusion. (See ref 85 for a plot of the diffusive evolution of $G(\theta, t)$ and further discussion of this function.) Comparison of the observed distributions (solid curves) to diffusion predictions (dashed curves) indicate that there is more large-amplitude rotation present than for pure diffusion, but the deviations are modest. In contrast, the evolution of the x (and y) distributions clearly deviate from diffusion predictions. These latter distributions resemble those computed by Shim and Kim for reorientation of diatomic solutes in an ionic liquid.⁸⁵ Simultaneous to increases in probability at small angles, there is a build-up of probability at larger angles and a second peak appearing in the distribution at 180° . (The fact that a peak occurs at 180° is more obvious from a plot of the distributions in $\cos \theta$ rather than θ , but the shapes of the $\cos \theta$ distributions are generally less revealing.) Thus both small-

amplitude diffusive motions and large-amplitude jump motions contribute to reorientation of the x and y molecular axes.

The nature of this rotational motion is further illustrated by the representative angular trajectories shown in Figure 13. Here we switch back to examining rotations about the z axis (φ_z), which are responsible for reorientation of the x and y axes. The trajectories in Figure 13 were recorded at 350 K, the lowest temperature studied, where the distinction between the two types of motion is most dramatic, but comparable features are present at all temperatures. A strong preference for large-angle displacements of 180° (π jumps) is evident in these trajectories. Not infrequently one finds two or even three 180° jumps (no. 5) occurring in rapid succession. The preference for 180° jumps results from the small moment of inertia for z -axis rotation and the quasi-linear shape of the cation. Such jumps are interspersed among periods of small-amplitude librational oscillations of 5 – 15° as well as slower diffusive angular variations which are seen most clearly in trajectories no. 1 and no. 4, where jumps are infrequent. Also evident from the random sampling of six trajectories in Figure 13 is the heterogeneous nature of z -axis rotation. For example, during the 2 ns period sampled, cation no. 1 undergoes only a single 360° jump of ~ 10 ps duration (returning to its initial orientation), whereas in this same time period cation no. 3 makes over 30 large-amplitude jumps. Trajectory no. 6 provides an example of an atypical (but not rare) type of motion wherein rotation has a persistent direction. The larger librational amplitude ($\sim 30^\circ$) of this trajectory suggests that this cation exists in a larger than average cavity. But the reason for such persistent unidirectional motion is not clear at present. Habasaki and Ngai observed similarly persistent translational motions in ionic liquid simulations⁸² and suggested that long-range and long-time-scale correlations must be involved. Whatever their origin, such atypically fast molecules, whether or not the motion is unidirectional, have a large impact on the orientational MSDs and diffusion coefficients determined from them.

A simple calculation based on the data in Figure 13 serves to explain why the heterogeneity of orientational motions, together with the propensity for intermittent 180° jumps, leads to rotational diffusion coefficients that apparently report much faster rotational motion than do correlation functions of the principal axis directions (Figures 8 and 9), especially at low temperatures. Consider, for example, the value of φ_z^2 averaged over the set of trajectories shown in Figure 13 at some arbitrary time, for example, 2 ns. The average value of φ_z^2 over the five “typical” trajectories shown here is $6.5\pi^2$. Inclusion of the “atypical” trajectory no. 6 increases this value to $22\pi^2$. The occurrence of fast molecules raises the full ensemble averaged value of $\langle \varphi_z^2 \rangle$ even further—the value read from Figure 8 is $131\pi^2$. Thus “atypical” molecules dominate in determining $\langle \varphi_z^2 \rangle$, and if one uses the ensemble-averaged rms value, or, equivalently, the diffusion coefficient, to gauge the “average” extent of motion, reorientation angles of $11\pi = 2100^\circ$ result, when in fact a typical value of $|\varphi_z|$ is roughly 5-fold smaller. Now consider the extent of rotational motion based on the correlation functions $C_i^{(L)}(t)$. The same six trajectories observed at $t = 2$ ns yield averages of $P_1(\cos \varphi_z) = 0.50$ and $P_2(\cos \varphi_z) = 0.40$, respectively. These values can be interpreted as the z -axis contributions to reorientation of the x and y axes. If one inverts the Legendre polynomials to obtain “average” rotation angles from the correlation functions, one finds values of 60° ($L = 1$) and 55° ($L = 2$). The corresponding x/y average values obtained from the correlation functions in Figure 9 are 74° and 55° —orders of magnitude smaller than the value of $(\langle \varphi_z^2 \rangle)^{1/2}$.

Thus, the same set of $\varphi_z(t)$ trajectories interpreted from the perspectives of rotational MSDs versus orientational correlation functions provide very different answers. The two only yield similar results when 180° rotations do not dominate the motion and when the system is not strongly heterogeneous. In the present ionic liquid model, these conditions are not fulfilled even at the highest temperature studied, which is why a ~ 6 -fold discrepancy between the rotational correlation times and estimates of these times remains (Figures 8 and 9) even at high temperatures. The same is not true in the case of the neutral liquid mixture we examine in the following section.

5. Effect of Electrostatic Interactions on Dynamics

To obtain more insight into how the distinctive dynamics described above are related to the strong electrostatic interactions present in the ionic liquid, we also simulated a neutral mixture in which the Lennard-Jones parameters of the original model were maintained but all charges removed. For convenience, we will refer to the original ionic liquid model as “IL” and this neutral mixture as “NM”. We focus mainly on comparisons of the IL and NM systems at 450 K and at the same density as the IL, using *NVT* simulations for the latter system.¹⁰¹ By comparing equal densities we can better isolate the effects of electrostatics on the structure and dynamics.

Before making such isodensity comparisons, the comparisons at atmospheric pressure listed in Table 2 can first be used to appreciate some of the characteristic differences between ionic liquids and conventional solvents. Because the NM is gaseous at 450 K and atmospheric pressure, the data in Table 2 are for 298 K, but the difference in temperature is unimportant for the comparisons made here. In the absence of electrostatic interactions, the Lennard-Jones parameters chosen for the IL lead to both static and dynamic properties of the NM that are similar to those of conventional organic solvents. For example, for *n*-hexane (298 K, 1 bar) the values of the quantities summarized in Table 1 are as follows: $V_m = 1.32 \times 10^{-4} \text{ m}^3 \text{ mol}^{-1}$, $\kappa_T = 1.7 \text{ GPa}^{-1}$, $\Delta_{\text{vap}}H = 31.5 \text{ kJ mol}^{-1}$, $D = 4.2 \times 10^{-9} \text{ m}^2 \text{ s}^{-1}$, and $\eta = 0.29 \text{ mPa s}^{-1}$, all close to the values calculated for the NM. (Note that these molar hexane quantities must be multiplied by a factor of 2 for comparison to the Table 2 results.¹⁰²) Comparison of the IL properties extrapolated to 298 K and the NM data shows that electrostatic interactions increase the density of the liquid by 26% and decrease the compressibility by a factor of 4. This simulated density increase is larger than the 19% change reported in the experimental comparison of a pyrrolidinium ionic liquid and its neutral counterpart by Shirota and Castner.⁵⁵ Given the additional fact that the simulated compressibility of the IL model is lower than is typical of ILs, it is likely that these volume changes are exaggerated in the present model compared to real systems.

As far as dynamics go, the differences between the IL and NM are huge. Although we do not have reliable measurements of viscosities or diffusion coefficients in the IL at 298 K, it is clear that the fluidity of the liquid, as reflected in the latter properties, decreases by more than 1000-fold when electrostatic interactions are included. These changes are no doubt exaggerated by the simplified model studied here. Shirota and Castner observed only a 30-fold change in viscosity and in the time of the slowest component of anisotropy relaxation in their experiments.⁵⁵ A final interesting feature of the above comparisons is how different are the predictive abilities of the NM and IL models for dynamics. Whereas the NM model possesses viscosities and diffusivities representative of conventional organic solvents, the dynamics in the IL model only compare

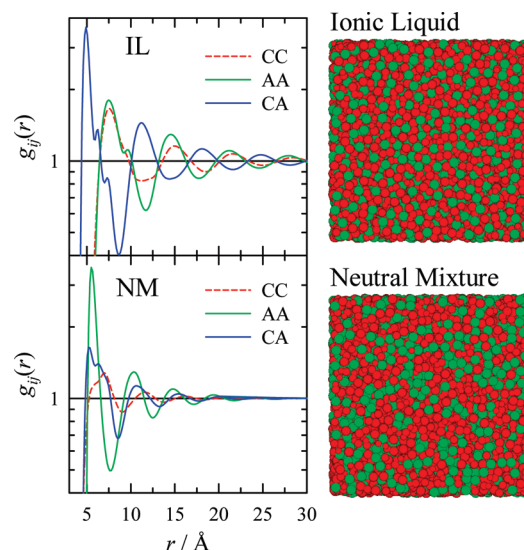


Figure 14. Comparison of structural features of the ionic liquid and neutral mixture models at 450 K. The graphs on the left are center of mass distribution functions. The vertical axes are logarithmic and span the range of 0.4–4. The panels at the right show snapshots of simulation boxes (2744 C–A pairs) of these two systems. Red indicates C and green A.

to realistic IL systems after a temperature shift of ~ 100 K. This difference suggests that simulation of ionic liquids places much greater demands on the realism of potential models than do conventional solvents.

We now turn to comparisons at constant density, where the presence of electrostatic interactions alone determines any differences observed between the NM and IL systems. Figure 14 serves to highlight the structural differences between the two systems. The graphs on the left of Figure 14 compare the center-of-mass radial distribution functions of the two systems, and Table S1 of the Supporting Information lists coordination numbers obtained from these functions. On the basis of these rdfs, the NM appears considerably less structured than the IL at large r . If, however, one looks not at the individual $g_{ij}(r)$ functions but at net density distributions independent of molecular identity (see Figure S3 of the Supporting Information), the density ordering caused by a central molecule is comparable in the two systems; in fact the NM appears more ordered at long range. What is dramatically different between the two systems is that the species alternation C–A–C–A..., clearly visible in the IL radial distribution functions and quantified by the charge distribution function $Q(r)$ in Figure 4, is absent in the NM. (See Figure S3.) A visual sense of the charge ordering present in the IL is provided by the simulation snapshots on the right side of Figure 14. Whereas the NM exhibits the sort of random fluctuations in composition expected for a 1:1 mixture of C and A,¹⁰³ in the IL C and A ions are each distributed in a highly uniform manner. This visualization suggests that it is fruitful to think of the IL as consisting of a distorted lattice structure of interleaved cation and anion arrays. In contrast to the NM where repulsive (packing) and entropic forces dominate, the strong electrostatic interactions, which demand a high penalty for improper charge balance, dictate the structure of the IL. While these observations are unsurprising, the influence that this charge-induced structure exerts on dynamics in ionic liquids has been little discussed in the literature.

We now use comparisons between the dynamics observed in the IL and NM systems to explore this influence. Some qualitative comparisons of dynamics are provided in Figure 15.

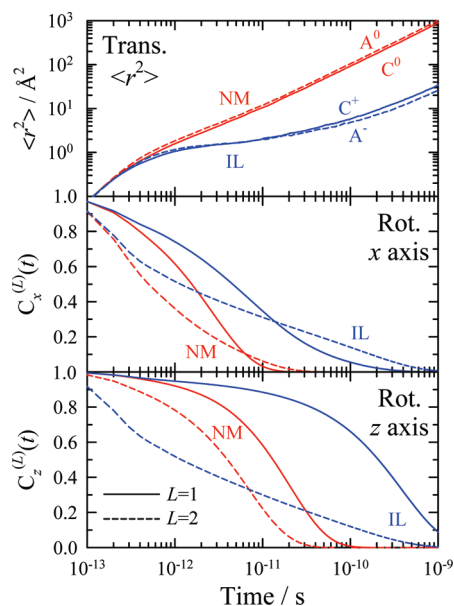


Figure 15. Comparison of various dynamics in the ionic liquid and corresponding neutral mixture systems at 450 K. The top panel shows translational mean square displacements of C and A species and the bottom two panels rotational correlation functions of the x and y molecular axes.

As would be anticipated, in all cases the corresponding dynamics in the NM are much faster than in the IL. Dynamics in the NM also tend to be simpler. The translational MSDs of the NM (top panel of Figure 15) do not display a pronounced subdiffusive region characteristic of supercooled liquids as does the IL. In the NM there is no clear-cut separation between the time scales of caged motions and diffusive reorganization even at 350 K, whereas large-amplitude motions in the IL are arrested for tens of nanoseconds at this temperature. There are other aspects of the dynamics that indicate the NM is a normal liquid with regard to dynamics. In contrast to the highly non-Arrhenius temperature dependence of viscosity and D_{tr} of the IL shown in Figure 5, in the NM these quantities can be well-fit to simple Arrhenius forms over the range of 350–450 K. Finally, the non-Gaussian parameters $\alpha_{\text{trans}}(t)$ and $\alpha_{\text{rot}}(t)$ in the NM are much smaller (<0.2) than those of the IL (Figure 10) and do not indicate the presence of significant dynamic heterogeneity. These comparisons at equal density demonstrate that it is not merely the higher densities of ionic liquids compared to conventional liquids that lead to more complex and heterogeneous dynamics. Rather, the fact that the dynamics of ionic liquids are similar to those of supercooled liquids must be a more direct result of the presence of strong ionic interactions.

Some more quantitative comparisons between dynamics in the IL and NM can be made on the basis of the data in Table 4. As listed there, the viscosity of the NM is 1.1 mPa s, a value 75 times smaller than that of the IL. The column labeled “rate ratio” in Table 4 documents how the single-molecule dynamics differ in these two systems. Accompanying the much greater fluidity of the NM, the translational diffusion coefficients and rotational correlation times change by factors of 20–40, a change of roughly one-third to half of the change in viscosity. The same is not true of the rotational diffusion coefficients, all of which increase by much smaller factors in going from the IL to the NM. This small change is due primarily to the anomalously large values of D_{rot} in the IL discussed previously.

More details on hydrodynamic predictions for the NM are provided in Table 3. Here one sees that the translational diffusion

TABLE 4: Comparison of Dynamics in the IL, NM, and q^0/IL Systems (450 K)^a

motion	quantity	NM		q^0/IL	
		value	rate ratio	value	rate ratio
viscosity	$\eta/(\text{mPa s})$	1.1	75	81	1.0
Translational Diffusion Coefficients					
A^0	$D_A/(10^{-11} \text{ m}^2 \text{ s}^{-1})$	170	43	17	4.4
C^0	$D_C/(10^{-11} \text{ m}^2 \text{ s}^{-1})$	150	29	18	3.4
Cation (C^0) Rotational Correlation Times					
rotation of x	$\tau_x^{(1)}/\text{ps}$	2.6	10	4	8
rotation of x	$\tau_x^{(2)}/\text{ps}$	2.3	28	12	5
rotation of y	$\tau_y^{(1)}/\text{ps}$	2.6	10	4	7
rotation of y	$\tau_y^{(2)}/\text{ps}$	2.1	24	7	7
rotation of z	$\tau_z^{(1)}/\text{ps}$	20	22	40	10
rotation of z	$\tau_z^{(2)}/\text{ps}$	6.6	33	40	6
Cation (C^0) Rotational Diffusion Coefficients					
rotation about x	$D_x/(10^{10} \text{ s}^{-1})$	3.4	3.2	4.1	3.9
rotation about y	$D_y/(10^{10} \text{ s}^{-1})$	3.2	3.1	4.1	4.0
rotation about z	$D_z/(10^{10} \text{ s}^{-1})$	40	2.9	66	4.8

^a Observed quantities are listed in the columns labeled “value” and ratios of the observed rates (or $1/\text{times}$) to those in the IL are listed in the columns labeled “rate ratio”. “NM” denotes simulations in which all charges are zero and “ q^0/IL ” denotes a system in which the charges on five cations and anions are made zero in the presence of 338 ion pairs. In all cases the values listed refer to motion of uncharged species C^0 and A^0 , and the ratios are to rates of motion of C^+ and A^- in the pure IL. Uncertainties in the NM ratios are expected to be $<15\%$.

coefficients, rotation times, and rotational diffusion coefficients observed in the NM all fall within a factor of 3 of slip hydrodynamic predictions. Poorest agreement with such predictions occurs when rotations about the z molecular axis are involved, i.e., for τ_x , τ_y , and D_z . In the remaining cases the hydrodynamic predictions are remarkably accurate—on average only 30% lower than simulated values. Poorer performance when z -rotations are involved is due to the prevalence of the large-amplitude (180°) jumps about the z axis in the IL (Figure 13) and NM alike. Such jumps, facilitated by the quasi-linear structure of C molecules, also causes the crossing of the $C_{xy}^{(1)}(t)$ and $C_{xy}^{(2)}(t)$ correlation functions in both the NM and IL, as shown in Figure 15. But in the case of the NM, the presence of such nondiffusive rotations does not lead to the same dramatic departures from hydrodynamic predictions for the rotational diffusion coefficients as it does in the IL. In contrast to the decoupling between the D_i and viscosity seen in the IL (Figure 9), the temperature dependence of all of the NM rotational diffusion coefficients can be fit to $D_i = D_{0i}(\eta/T)^{-p}$ with $0.72 \leq p \leq 0.80$. While these exponents are smaller than for the D_{trans} and τ_{rot} , which are near unity, the behavior of the rotational diffusion coefficients is much closer to hydrodynamic expectations. Furthermore, whereas the connections between the $\{D_i\}$ and correlation times deduced from the small-step diffusion relations (eqs 12–14) are grossly inaccurate in the IL, especially at low temperatures (Figure 8), they hold to within about 30% in the NM case. This difference in behavior of the rotational diffusion coefficients can be traced to the heterogeneity of rotational motion and the presence of persistent fast rotators in the IL, as discussed in the previous section. Fast, large-amplitude rotations are also present in the NM, but it is the time scale separation between these rotational motions and structural reorganization in the IL that makes relatively atypical rotators dominate the rotational MSDs and diffusion coefficients. Such

effects lose prominence when structural reorganization and rotation occur on comparable time scales, as they do in the NM.

We finally examine how important direct electrostatic interactions between a molecule and its environment are in determining its dynamics. For this purpose we performed one additional simulation in which 5 out of the 343 ion pairs in the IL were turned into uncharged solutes, i.e., into the C^0 and A^0 of the NM system. The system was again at 450 K and held at the same volume as the IL. Inclusion of 5/343 or 1.5 mol % of neutral solutes into the IL is not expected to alter its properties significantly, an expectation supported by the observation that the diffusion coefficients and rotation times of the charged components C^+ and A^- in this solution all fall within a few percent of their values in the neat IL. Measures of the dynamics of the uncharged solutes in these simulations are listed in the columns labeled “ q^0/IL ” in Table 4. As seen from the rate ratios provided, translation diffusion of A^0 and C^0 are about 4-fold faster than their charged counterparts in the IL. The difference in rotation times is somewhat greater. By these measures, rotation of C^0 is about 8 times faster than rotation of C^+ . We will leave detailed analysis of such differences to future studies of solute dynamics, but it is likely that the 4- or 8-fold effects seen here can be ascribed to the greater friction on charged versus neutral solutes caused by electrostriction in the first solvation shell of ionic solutes.¹⁰⁴ (An example of electrostriction is provided in the distribution functions in Figure 14, where one sees that the first peak of $g_{CA}(r)$ in the IL lies at a smaller r than do the peaks of any of the $g_i(r)$ in the NM.) What is clear from comparison of the present IL, NM, and q^0/IL results is that the primary effect of electrostatic interactions, especially on translational motions, comes through their retardation of structural reorganization, as reflected in the 75-fold greater viscosity of the IL compared to the NM. This retardation in turn reflects the difficulty in rearranging the ionic-lattice-like structure of the IL, which presumably requires cooperative motion of large collections of ions. We suggest that it is this requirement of cooperative reorganization, enforced by strong charge–charge interactions, that makes dynamics in ionic liquids resemble those of supercooled liquids.

6. Summary and Conclusions

In this work we proposed an idealized model of an ionic liquid for simulation of solvation phenomena on the nanosecond time scales. The model was chosen to have properties resembling those of the prototypical ionic liquid 1-butyl-3-methylimidazolium hexafluorophosphate, $[Im_{41}][PF_6]$. It consists of only four interaction sites, one for the anion and three for the cation, compared to 32 sites in an all-atom representation of this same ionic liquid. This model economy enables simulation of dilute solute dynamics for hundreds of nanoseconds, facilitating future comparison to experiments on solvation dynamics and charge-transfer phenomena which are impractical with more realistic solvent models.

Although $[Im_{41}][PF_6]$ was used as a guide, it was not expected that such a simple model could closely match the properties of any specific ionic liquid, and therefore no real optimization was attempted. Instead, our hope was that reasonable parameter choices would lead to a generic model whose properties fell within the range found in the ionic liquids used in our experimental work.¹⁰⁵ This hope was only partially realized by the present model. Apart from the thermal expansion coefficient, which was found to be $\sim 30\%$ smaller than average ionic liquid values, the volumetric, structural, and energetic properties of the model liquid all appeared to fall within the ranges typically

observed in experiments or more realistic simulations of ionic liquids. But large discrepancies were found for dynamical properties such as viscosity and diffusion coefficients. At 350 K, where direct comparison to $[Im_{41}][PF_6]$ could be made, self-diffusion coefficients of the model liquid are ~ 100 -fold smaller than experimental values. The temperature dependence of these diffusion coefficients and the viscosity of the model are, however, quite similar to those of $[Im_{41}][PF_6]$. We found that the temperature-dependent dynamics of $[Im_{41}][PF_6]$ are nicely reproduced by the model when it is simulated at 100–110 K higher temperatures compared to experiment. The presence of this 100 K offset from experiment is disappointing, but not surprising given the fact that comparable discrepancies are sometimes found even with all-atom models.³¹ Without reducing the ion charges^{30,106,32} or adding explicit polarizability,^{107,108} neither of which seemed desirable at this point, it did not appear possible to significantly improve agreement with experiment by varying the parameters of the present model. For now at least, we decided to accept this discrepancy and account for the 100 K offset when making comparisons to experiment.

As already found using more sophisticated models,^{81,72,97,82} the dynamics of this model ionic liquid showed many of the characteristics typically associated with liquids in the supercooled regime. At model temperatures relevant to room-temperature experiments, translational motions remain subdiffusive for hundreds of picoseconds, during which time only caged motions are allowed and little restructuring of local environments occurs. At longer times on the order of 1 ns, large amplitude displacements (jumps) occur together with cage reformation. On both of these time scales, translational and rotational motions are heterogeneous; i.e., different molecules move at different rates depending on their local environment. Translational diffusion coefficients track shear viscosity approximately in the manner expected from simple hydrodynamics, $D_{CA} \propto (T/\eta)^p$ with p near unity. Moreover, both D_C and D_A can be predicted with reasonable accuracy using simple slip hydrodynamic calculations. These observations regarding translation motion are in good agreement with what is found for experimental diffusion coefficients.^{79,94,95,83} Similar proportionality to $(\eta/T)^p$ with p near unity is also observed for cation rotational correlation times, but only rotation times of the long molecular axis (z) are close to slip predictions. Rather different and apparently contradictory behavior was found for the rotational diffusion coefficients. These coefficients are all much larger than expected from hydrodynamic calculations, and they appear to decouple from viscosity at low temperatures. Similar decoupling between rotational and translational diffusion coefficients was also recently noted in a model of supercooled *o*-terphenyl.⁸⁴ In the present system, the unusual behavior of the rotational diffusion coefficients was traced to the propensity for 180° jumps about the z axis coupled to the strong effect dynamic heterogeneity has on mean-squared angular displacements. Although the quasi-linear character of the model cation, which makes such jump motions favorable, might be considered unrealistic, we note that the rotational dynamics observed in the present system bear considerable resemblance to those recently reported for a more realistic model of 1-ethyl-3-methylimidazolium in simulations of neat $[Im_{21}][PF_6]$.⁴³

To gain perspective on the interesting dynamics observed in the model ionic liquid (IL) it proved useful to make comparisons to two reference systems: molten NaCl and to a “neutral mixture” (NM) made by zeroing the charges of the IL model. At least as far as center-of-mass distribution functions are concerned, the structure of the model IL was found to differ

little from that of molten NaCl ($T_f = 1081$ K). Whereas one might think of NaCl as having greater ionic character than a typical room-temperature ionic liquid, the ratio of the ion–ion interaction energies to thermal energies, $q^2\rho^{1/3}/(4\pi\epsilon_0 k_B T)$, is actually slightly larger in the IL than in NaCl: ~ 51 for the model IL at 450 K versus ~ 50 in NaCl(T_f). In this sense, and given the fact that the model ions are relatively simple and comparable in size, the resemblance to NaCl, especially with regard to charge ordering, is not surprising. The homogeneous distribution of positive and negative charge required by strong electrostatic interactions leads to the impression of a distorted latticelike structure in both liquids. While the simplicity of the present model might make this structure more apparent, for any ionic liquid composed of ions of size comparable to $[\text{Im}_{41}][\text{PF}_6]$ the energetics of ion–ion interactions are comparable and thus the drive for charge balance and a homogeneous distribution of charge is equally strong. This feature of ionic liquids has not been stressed in prior simulation studies, which have more often highlighted the aggregation of polar and nonpolar groups that occurs especially when long alkyl chains are present.^{52,109,110,50} But we believe that this underlying structure and the coupling among ions it reflects is the main reason why the dynamics in ionic liquids, at least those with short alkyl chains such as $[\text{Im}_{41}][\text{PF}_6]$, resemble the dynamics of supercooled liquids. As already shown by the insightful experimental comparison of Shirota and Castner,⁵⁵ ion–ion interactions in ionic liquids lead to a substantial increase in density relative to corresponding liquid mixtures devoid of charge. But the analogous IL–NM comparisons performed here show that it is not the densification that is primarily responsible for the dramatic slow-down of the dynamics in ILs. Rather it is the structural rigidity of the electrostatic coupling that gives rise to the high viscosities and slow dynamics characteristics of ionic liquids. The similarity of the molecular motions in ionic liquids to those found in supercooled liquids presumably reflects the long-range nature of this coupling.

Acknowledgment. This work was funded by the Division of Chemical Sciences, Geosciences, and Biosciences, Office of Basic Energy Sciences of the U.S. Department of Energy through Grant DE-FG02-89ER14020. D.R. also thanks Chet Swalina for his help while beginning these simulations.

Supporting Information Available: Figures summarizing the simulated diffusion coefficients of $[\text{Im}_{41}][\text{PF}_6]$ from literature sources (Figure S1), a simulated cooling scan indicating an approximate glass transition temperature for the model IL (Figure S2), and a comparison of total density distributions of the IL and NM systems (Figure S3) and a table comparing coordination numbers in the IL and NM systems (Table S1). This material is available free of charge via the Internet at <http://pubs.acs.org>.

References and Notes

- Wishart, J. F.; Castner Edward, W., Jr. *J. Phys. Chem. B* **2007**, *111*, 4639.
- Rogers, R. D.; Voth, G. A. *Acc. Chem. Res.* **2007**, *40*, 1077.
- Plechikova, N. V.; Seddon, K. R. *Chem. Soc. Rev.* **2008**, *37*, 123.
- Wasserscheid, P.; Welton, T., Eds. *Ionic Liquids in Synthesis*, 2nd ed.; Wiley-VCH: Weinheim, Germany, 2008.
- Wishart, J. F. *Energy Environ. Sci.* **2009**, *2*, 956.
- Ionic Liquids in Chemical Analysis*; Koel, M., Ed.; CRC Press: Boca Raton, FL, 2009.
- Armand, M.; Endres, F.; MacFarlane, D. R.; Ohno, H.; Scrosati, B. *Nat. Mater.* **2009**, *8*, 621.
- Soukup-Hein, R. J.; Warnke, M. M.; Armstrong, D. W. *Annu. Rev. Anal. Chem.* **2009**, *2*, 145.
- Hunt, P. A. *Mol. Simul.* **2006**, *32*, 1.
- Lynden-Bell, R. M.; Del Pópolo, M. G.; Youngs, T. G. A.; Kohanoff, J.; Hanke, C. G.; Harper, J. B.; Pinilla, C. C. *Acc. Chem. Res.* **2007**, *40*, 1138.
- Padua, A. A. H.; Costa Gomes, M. F.; Lopes, C. J. N. A. *Acc. Chem. Res.* **2007**, *40*, 1087.
- Wang, Y.; Jiang, W.; Yan, T.; Voth, G. A. *Acc. Chem. Res.* **2007**, *40*, 1193.
- Shim, Y.; Jeong, D.; Manjari, S.; Choi, M. Y.; Kim, H. J. *Acc. Chem. Res.* **2007**, *40*, 1130.
- Kobrak, M. N. *J. Chem. Phys.* **2007**, *127*, 184507/1.
- Hu, Z.; Margulis, C. J. *Acc. Chem. Res.* **2007**, *40*, 1097.
- Bhargava, B. L.; Balasubramanian, S.; Klein, M. L. *Chem. Commun. (Cambridge, U. K.)* **2008**, 3339.
- Shimizu, K.; Costa Gomes, M. F.; Padua, A. A. H.; Rebelo, L. P. N.; Canongia Lopes, J. N. *J. Phys. Chem. B* **2009**, *113*, 9894.
- Maginn, E. J. *J. Phys.: Condens. Matter* **2009**, *21*, 373101.
- Urahata, S. M.; Ribeiro, M. C. C. *J. Chem. Phys.* **2004**, *120*, 1855.
- Liu, Z.; Huang, S.; Wang, W. *J. Phys. Chem. B* **2004**, *108*, 12978.
- Canongia Lopes, J. N.; Deschamps, J.; Padua, A. A. H. *J. Phys. Chem. B* **2004**, *108*, 2038.
- Canongia Lopes, J. N.; Padua, A. A. H.; Shimizu, K. *J. Phys. Chem. B* **2008**, *112*, 5039.
- Koeddermann, T.; Paschek, D.; Ludwig, R. *ChemPhysChem* **2007**, *8*, 2464.
- Maginn, E. J. *Rev. Comput. Chem.* **2009**, *26*, 421.
- Sambasivarao, S. V.; Acevedo, O. *J. Chem. Theory Comput.* **2009**, *5*, 1038.
- Borodin, O. *J. Phys. Chem. B* **2009**, *113*, 11463.
- Hanke, C. G.; Price, S. L.; Lynden-Bell, R. M. *Mol. Phys.* **2001**, *99*, 801.
- de Andrade, J.; Boees, E. S.; Stassen, H. *J. Phys. Chem. B* **2002**, *106*, 13344.
- Shah, J. K.; Brennecke, J. F.; Maginn, E. J. *Green Chem.* **2002**, *4*, 112.
- Bhargava, B. L.; Balasubramanian, S. *J. Chem. Phys.* **2007**, *127*, 114510/1.
- Tsuzuki, S.; Shinoda, W.; Saito, H.; Mikami, M.; Tokuda, H.; Watanabe, M. *J. Phys. Chem. B* **2009**, *113*, 10641.
- Lynden-Bell, R. M.; Youngs, T. G. A. *J. Phys.: Condens. Matter* **2009**, *21*, 424120.
- Micaelo, N. M.; Baptista, A. M.; Soares, C. M. *J. Phys. Chem. B* **2006**, *110*, 14444.
- Wu, X.; Liu, Z.; Huang, S.; Wang, W. *Phys. Chem. Chem. Phys.* **2005**, *7*, 2771.
- Chaumont, A.; Wipff, G. *Inorg. Chem.* **2009**, *48*, 4277.
- Kerle, D.; Ludwig, R.; Geiger, A.; Paschek, D. *J. Phys. Chem. B* **2009**, *113*, 12727.
- Arzhantsev, S.; Jin, H.; Baker, G. A.; Maroncelli, M. *J. Phys. Chem. B* **2007**, *111*, 4978.
- Jin, H.; Baker, G. A.; Arzhantsev, S.; Dong, J.; Maroncelli, M. *J. Phys. Chem. B* **2007**, *111*, 7291.
- Jin, H.; Li, X.; Maroncelli, M. *J. Phys. Chem. B* **2007**, *111*, 13473.
- Margulis, C. J. *Mol. Phys.* **2004**, *102*, 829.
- Shim, Y.; Choi, M. Y.; Kim, H. J. *J. Chem. Phys.* **2005**, *122*, 044511.
- Bhargava, B. L.; Balasubramanian, S. *J. Chem. Phys.* **2005**, *123*, 144505/1.
- Shim, Y.; Kim, H. J. *J. Phys. Chem. B* **2008**, *112*, 11028.
- Streeter, I.; Lynden-Bell, R. M.; Compton, R. G. *J. Phys. Chem. C* **2008**, *112*, 14538.
- Annapureddy, H. V. R.; Hu, Z.; Xia, J.; Margulis, C. J. *J. Phys. Chem. B* **2008**, *112*, 1770.
- Song, X. *J. Chem. Phys.* **2009**, *131*, 044503.
- Lynden-Bell, R. M. *J. Phys. Chem. B* **2007**, *111*, 10800.
- Shim, Y.; Kim, H. J. *J. Phys. Chem. B* **2009**, *113*, 12964.
- Annapureddy, H. V. R.; Margulis, C. J. *J. Phys. Chem. B* **2009**, *113*, 12005.
- Bhargava, B. L.; Devane, R.; Klein, M. L.; Balasubramanian, S. *Soft Matter* **2007**, *3*, 1395.
- Raju, S. G.; Balasubramanian, S. *J. Phys.: Condens. Matter* **2009**, *21*, 035105/1.
- Wang, Y.; Voth, G. A. *J. Am. Chem. Soc.* **2005**, *127*, 12192.
- Wang, Y.; Feng, S.; Voth, G. A. *J. Chem. Theory Comput.* **2009**, *5*, 1091.
- Wang, Y.; Izvekov, S.; Yan, T.; Voth, G. A. *J. Phys. Chem. B* **2006**, *110*, 3564.
- Shirota, H.; Castner, E. W., Jr. *J. Phys. Chem. A* **2005**, *109*, 9388.
- Morrow, T. I.; Maginn, E. J. *J. Phys. Chem. B* **2002**, *106*, 12807.
- Smith, W.; Forester, T. R., Eds. *DL-POLY_2.13*; CCLRC Daresbury Laboratory: Daresbury, U.K., 2001.
- Allen, M. P.; Tildesley, D. J. *Computer Simulation of Liquids*; Oxford University Press: Oxford, U.K., 1987.

- (59) Frenkel, D.; Smit, B. *Understanding Molecular Simulation, from Algorithms to Applications*, 2nd ed.; Academic Press: New York, 2002.
- (60) Kelkar, M. S.; Maginn, E. J. *J. Phys. Chem. B* **2007**, *111*, 9424.
- (61) Leal, J. P.; Esperanca, J. M. S. S.; Da Piedade, M. E. M.; Lopes, J. N. C.; Rebelo, L. P. N.; Seddon, K. R. *J. Phys. Chem. A* **2007**, *111*, 6176.
- (62) Chen, T.; Smit, B.; Bell, A. T. *J. Chem. Phys.* **2009**, *131*, 246101/1.
- (63) Schröder, C.; Wakai, C.; Weingärtner, H.; Steinhäuser, O. *J. Chem. Phys.* **2007**, *126*, 84511.
- (64) Helfand, E. *Phys. Rev.* **1960**, *119*, 1.
- (65) Machida, H.; Sato, Y.; Smith, R. L., Jr. *Fluid Phase Equilib.* **2008**, *264*, 147.
- (66) Gardas, R. L.; Coutinho, J. A. P. *AIChE J.* **2009**, *55*, 1274.
- (67) Janz, G. J. *Thermodynamic and Transport Properties for Molten Salts: Correlation Equations for Critically Evaluated Density, Surface Tension, Electrical Conductance, and Viscosity Data*; American Institute of Physics: New York, 1988.
- (68) Edwards, F. G.; Enderby, J. E.; Howe, R. A.; Page, D. I. *J. Phys. C* **1975**, *8*, 3483.
- (69) Koblinski, P.; Eggebrecht, J.; Wolf, D.; Phillpot, S. R. *J. Chem. Phys.* **2000**, *113*, 282.
- (70) In Figure 4 we approximate the $Q(r)$ using center of mass rdfs, which effectively places all of the cation charge at the center of mass. We have also calculated the more proper functions which account for the distribution of charge within the cations. These functions differ very little after the first 10 Å.
- (71) As described by Lynden-Bell,¹¹¹ the electrostatic potential surrounding a central ion can be determined from an integral over $Q(r)$. Although screening greatly reduces the electrostatic interaction between two ions compared to the bare Coulomb interaction, the remaining oscillations in the electrical potential still amount to ~ 0.2 eV, or energies in excess of $5 k_B T$, out to distances of 20–25 Å. These distances imply substantial coupling among ~ 200 ions.
- (72) Del Pópolo, M. G.; Voth, G. J. *J. Phys. Chem. B* **2004**, *108*, 1744.
- (73) Armstrong, J. P.; Hurst, C.; Jones, R. G.; Licence, P.; Lovelock, K. R. J.; Satterley, C. J.; Villar-Garcia, I. J. *J. Phys. Chem. Chem. Phys.* **2007**, *9*, 982.
- (74) Liu, Z.; Wu, X.; Wang, W. *J. Phys. Chem. Chem. Phys.* **2006**, *8*, 1096.
- (75) Verevkin, S. P. *Angew. Chem., Int. Ed.* **2008**, *47*, 5071.
- (76) Deyko, A.; Lovelock, K. R. J.; Corfield, J.-A.; Taylor, A. W.; Gooden, P. N.; Villar-Garcia, I. J.; Licence, P.; Jones, R. G.; Krasovskiy, V. G.; Chernikova, E. A.; Kustov, L. M. *J. Phys. Chem. Chem. Phys.* **2009**, *11*, 8544.
- (77) *Landolt-Bornstein*, Series II; Springer-Verlag: Berlin, 1961; Vol. 4.
- (78) Koeddermann, T.; Paschek, D.; Ludwig, R. *ChemPhysChem* **2008**, *9*, 549.
- (79) Tokuda, H.; Kikuko, H.; Ishii, K.; Susan, M. A. B. H.; Watanabe, M. J. *J. Phys. Chem. B* **2004**, *108*, 16593.
- (80) Kob, W. *Lect. Notes Physics* **2006**, *704*, 1.
- (81) Margulis, C. J.; Stern, H. A.; Berne, B. J. *J. Phys. Chem. B* **2002**, *106*, 12017.
- (82) Habasaki, J.; Ngai, K. L. *J. Chem. Phys.* **2008**, *129*, 194501/1.
- (83) Tokuda, H.; Tsuzuki, S.; Susan, M. A. B. H.; Hayamizu, K.; Watanabe, M. J. *J. Phys. Chem. B* **2006**, *110*, 19593.
- (84) Lombardo, T. G.; Debenedetti, P. G.; Stillinger, F. H. *J. Chem. Phys.* **2006**, *125*, 174507/1.
- (85) Shim, Y.; Jeong, D.; Choi, M. Y.; Kim, H. J. *J. Chem. Phys.* **2006**, *125*, 061102.
- (86) Kämmerer, S.; Kob, W.; Schilling, R. *Phys. Rev. E* **1997**, *56*, 5450.
- (87) For hydrodynamic modeling⁸⁹ of the rotational motion of an asymmetric ellipsoid we use the relations provided by Perrin¹¹² for stick boundary conditions and interpolation of values tabulated by Youngren and Acrivos^{113,114} for slip boundary conditions. In the case of translation we use the methods described in the recent paper by Gordon¹¹⁵ for a prolate ellipsoid.
- (88) Favro, L. D. *Phys. Rev.* **1960**, *119*, 53.
- (89) Fleming, G. R. *Chemical Applications of Ultrafast Spectroscopy*; Oxford University Press: New York, 1986.
- (90) Harris, K. R. *J. Chem. Phys.* **2009**, *131*, 054503/1.
- (91) Horng, M.-L.; Gardecki, J.; Maroncelli, M. *J. Phys. Chem.* **1997**, *101*, 1030.
- (92) Zwanzig, R.; Harrison, A. K. *J. Chem. Phys.* **1985**, *83*, 5861.
- (93) Ediger, M. D. *Annu. Rev. Phys. Chem.* **2000**, *51*, 99.
- (94) Tokuda, H.; Hayamizu, K.; Ishii, K.; Susan, M. A. B. H.; Watanabe, M. J. *J. Phys. Chem. B* **2005**, *109*, 6103.
- (95) Tokuda, H.; Ishii, K.; Susan, M. A. B. H.; Tsuzuki, S.; Hayamizu, K.; Watanabe, M. J. *J. Phys. Chem. B* **2006**, *110*, 2833.
- (96) Kob, W.; Donati, C.; Plimpton, S. J.; Poole, P. H.; Glotzer, S. C. *Phys. Rev. Lett.* **1997**, *79*, 2827.
- (97) Hu, Z.; Margulis, C. J. *Proc. Natl. Acad. Sci. U.S.A.* **2006**, *103*, 831.
- (98) Koeddermann, T.; Ludwig, R.; Paschek, D. *ChemPhysChem* **2008**, *9*, 1851.
- (99) Shell, M. S.; Debenedetti, P. G.; Stillinger, F. H. *J. Phys.: Condens. Matter* **2005**, *17*, S4035.
- (100) Rahman, A. *Phys. Rev.* **1964**, *136*, 405.
- (101) In comparisons of the NM at 298 K as well as the IL at several temperatures, we found no significant differences between NVT and NPT simulations. Comparison of NPT simulations of the IL and NVT simulations of the NM are therefore appropriate.
- (102) The molar basis for the results in Table 2 is a mole of C + A pairs, whereas the basis for a single-component liquid such as *n*-hexane is a mole of molecules. To compare the NM with a single-component fluid, we ignore the distinction between C and A and take 1 mol of C + A pairs to be equivalent to 2 mols of “average” C/A molecules.
- (103) The snapshot of the NM in Figure 14 might give the impression of clustering of C (red) and A (green) molecules and perhaps even incipient phase separation. However, this impression is largely a visual trick resulting from the fact that each C molecule is comprised of three sites each colored red. The coordination numbers (Table S1) of this system show that distribution of C and A molecules in the NM is, in fact, random on average but with fluctuations in local compositions typical of a 50–50 mixture.
- (104) Kumar, P. V.; Maroncelli, M. *J. Chem. Phys.* **2000**, *112*, 5370.
- (105) Jin, H.; O'Hare, B.; Dong, J.; Arzhantsev, S.; Baker, G. A.; Wishart, J. F.; Benesi, A.; Maroncelli, M. *J. Phys. Chem. B* **2008**, *112*, 81.
- (106) Youngs, T. G. A.; Hardacre, C. *ChemPhysChem* **2008**, *9*, 1548.
- (107) Yan, T.; Burnham, C. J.; Del Pópolo, M. G.; Voth, G. A. *J. Phys. Chem. B* **2004**, *108*, 11877.
- (108) Borodin, O.; Smith, G. D. *J. Phys. Chem. B* **2006**, *110*, 11481.
- (109) Wang, Y.; Jiang, W.; Voth, G. A. *ACS Symp. Ser.* **2007**, *975*, 272.
- (110) Lopes, J. N. C.; Padua, A. A. H. *J. Phys. Chem. B* **2006**, *110*, 3330.
- (111) Lynden-Bell, R. M. *J. Chem. Phys.* **2008**, *129*, 204503/1.
- (112) Perrin, F. *Phys. Radium* **1934**, *5*, 497.
- (113) Youngren, G. K.; Acrivos, A. *J. Chem. Phys.* **1975**, *63*, 3846.
- (114) Sensen, R. J.; Hochstrasser, R. M. *J. Chem. Phys.* **1993**, *98*, 2490.
- (115) Gordon, P. A. *Ind. Chem. Eng. Res.* **2003**, *42*, 7025.